sustainability

MDPI

Article

Evolution of Iceberg A68 since Its Inception from the Collapse of Antarctica's Larsen C Ice Shelf Using Sentinel-1 SAR Data

Shivangini Singh [1], Shashi Kumar [1,*] and Navneet Kumar [2]

[1] Indian Institute of Remote Sensing (IIRS), ISRO, Dehradun 248001, India
[2] Department of Ecology and Natural Resources Management, Center for Development Research (ZEF), University of Bonn, Genscherallee 3, 53113 Bonn, Germany
* Correspondence: shashi@iirs.gov.in; Tel.: +91-812-615-2267

Abstract: This research focuses on the evolution of the largest iceberg A68 and analyzes the trajectory using Sentinel-1 SAR data. The monitoring began when A68 calved Larsen C Ice shelf on 12 July 2017, and ended on 1 February 2021. A total of 47 images were analyzed and studied to ascertain the changes in the area, trajectory and the factors that might have influenced said changes. The big size of the iceberg caught the scientific community's attention when it started moving towards South Georgia Island, a habitat of penguins and seals. The pattern of decrease and increase in the iceberg's size was analyzed and compared with the surrounding sea ice extent to account for longitudinal stretching and shrinkage. Iceberg's trajectory was also studied to take into account the underlying seabed and ice rises, and their implication on A68's maneuverability, giving rise to unique motions in the coastal regime. Two subsequent calving events in the iceberg were distinctly observed in March 2019 and April 2020. Since its inception up to December 2019, its drift was fairly gradual, with the pick up in pace observed upon its entry into open waters and departure from the peninsular region. The decrease in size was also fairly gradual with only two main calving events, as mentioned above. The cold water and sea ice surrounding the iceberg potentially helped maintain a steady state. Post its sojourn into the Southern Ocean, major calving began in December 2020 and continued through January 2021. This study explores the potential of SAR remote sensing in iceberg monitoring and tracking.

Keywords: iceberg A68; Sentinel-1 SAR; Larsen C ice shelf; iceberg monitoring

Citation: Singh, S.; Kumar, S.; Kumar, N. Evolution of Iceberg A68 since Its Inception from the Collapse of Antarctica's Larsen C Ice Shelf Using Sentinel-1 SAR Data. *Sustainability* **2023**, *15*, 3757. https://doi.org/10.3390/su15043757

Academic Editor: Jakub Brom

Received: 15 November 2022
Revised: 6 February 2023
Accepted: 15 February 2023
Published: 18 February 2023

1. Introduction

The calving of colossal tabular iceberg A68 from the Larsen C Ice Shelf in the Antarctic Peninsula in July 2017, resulted in an exclusive opportunity to study the evolution of a newly formed iceberg, ascertain its movement, and the factors influencing it and change in freeboard. The initial calving event resulted in a loss of ~6000 km^2 which represents 9–12% of the entire shelf. Although scientists had noticed A68's massive size since its July 2017 break away from the Larsen C Ice shelf, in November 2020, it attracted the attention of the scientific community to a worrying situation when it was found that A68 could hit the South Georgia island, posing a serious threat to the local penguins and seals if it did. Owing to the microwave radiation of SAR instruments, they provide the ability of cloud penetration and thus are far better suited for analysis in Polar Regions, in comparison to optical sensors. Iceberg evolution study is of key interest since it helps in: (1) understanding the role of ice shelf disintegration in climate change studies; (2) risk mitigation for marine navigation from drift study; and (3) determining the geophysical parameters that might influence wildlife. Icebergs as large as A68 can potentially play a pivotal role in ice shelf instability and may also give rise to further rifting in the structure. A combination of persistent cloud cover and the polar nights render optical sensors handicapped in providing consistent data from the Polar Regions. Spaceborne SAR remote sensing thus proves to be a valuable tool in overcoming these shortcomings, providing independence from dependability on the weather and illumination conditions. The study of iceberg trajectory and evolution modelling has been of wide interest to glaciologists and remote sensing experts alike since they provide valuable insights into the coastal makeup of continents (ice rises and bed shelf) and ice shelves.

Calving at glacier tongues and ice shelves along the coast, where glaciers terminate in the sea, produces icebergs. Icebergs have an impact on local water circulation and, as a result, the formation of sea ice. The movement of freshwater into the open sea is aided by iceberg drift, which forms thin layers of fresh melt water as it melts. In recent years, there has been an increase in interest in iceberg drift and decay and the consequential freshwater release as an integral component of Earth's climate system models. In addition, icebergs remain a threat to offshore drilling activities, shipping, and subsea pipelines. Many models have been hypothesized to explain iceberg drift and decay and the factors influencing it, which include wind, ocean currents, and bathymetry, to name a few. The rising trend in calving occurrences in the Antarctic and Arctic glaciers is being blamed on ongoing climate change [1–3]. The trend is expected to accelerate in the coming decades, playing a pivotal role in regional ecosystems and ocean circulation trends [4–6]. An improved understanding of iceberg dynamics has thus become more relevant in recent times.

Many studies have focused on iceberg decay processes and the associated freshwater release into high-latitude oceans [7–10]. Iceberg ablation processes can be compartmentalized into discrete and continuous. Fragmentation processes are usually discrete whereas thermodynamic processes are continuous and both depend upon environmental conditions, such as wave spectra, air and water temperatures, winds, and current velocities [11]. Insolation and convection due to wind cause above-water heat transfer and melting. Since the above-water volume of an iceberg constitutes only around 13% of the total iceberg volume, above-water ablation due to thermodynamic processes is comparatively minor. Underwater melting (melting occurring on the submerged portion of the iceberg) is caused by natural convection (convection currents caused due to temperature differences in the ocean water) due to the buoyant vertical plume of iceberg meltwater and forced convection due to the relative motion of the iceberg and the fluid surrounding it. Both are a function of water temperature. The meltwater formed around the iceberg is at a different temperature than the water already surrounding the iceberg. This differential temperature gives rise to convection currents, as well as a slightly more buoyant mass of meltwater. Accelerated melting near the free water surface may be caused by gravity waves incident on an iceberg. Wave erosion is also dependent on wave energy, hence it is sensitive to wave direction. Thermal-induced stress (from the difference in the iceberg's and the surrounding water's temperature) and hydrostatic and inertial forces cause fragmentation. Inertial forces are assumed to be inconsequential for large icebergs, such as A68. Reorientation through rolling may be caused by motion-induced stretches and are usually catastrophic. Stresses due to weight and buoyancy can split an iceberg in half. In a similar vein, bending moments due to the passage of waves can also cause splitting but this is probably only for large and irregularly shaped icebergs. Fragmentation events are initiated largely due to defects in the ice, large discontinuities and drainage channels, and crevasse effects. The capacity to (i) reproduce individual iceberg trajectories using dynamic hindcast models [12–14]; or (ii) anticipate trajectories using statistical associations obtained from observed trajectories has been stressed in many iceberg drift research. The 2% rule, which asserts that icebergs move at about 2% of wind velocity relative to ocean currents, is a well-established empirical rule of the statistical approach [15,16]. A study by Wagner points out a caveat in this rule: even though the analytical model's asymptomatic result is consistent with the empirical rule, in the case of large icebergs and weak winds, wind contribution to driving the iceberg trajectory becomes negligible, and it instead drifts with the surface current [17]. Small icebergs and high winds, however, follow the 2% rule, which states that icebergs drift at ~2% of surface winds relative to water. Even though the inclusion of an analytical model to study A68's drift is beyond the scope of this chapter, it is imperative to mention the bigger picture that I aim to ultimately understand for this behemoth.

A gigantic iceberg was calved from the Larsen C ice shelf in July 2017, named A68 by the National Ice Centre (NIC) [18]. At roughly 5800 km^2, it amounted to nearly 10% of the entire Larsen C ice shelf area. According to the NIC and Brigham Young University's consolidated iceberg tracking database, iceberg A68 is the sixth-biggest iceberg on satellite observation records overall, and the largest now (at the time of this study). While Parmiggiani and Moctezuma-Flores conducted a study on the SAR-based displacement study of A68 [19], much needs to be analyzed in terms of environmental factors and dealing with the random behavior of SAR data. The life cycle of an iceberg post a calving event from its parent ice shelf depends on several factors, the extent of sea ice surrounding the region, ocean currents and temperature, salinity, atmospheric conditions, namely temperature and wind speed, and topography of the underlying region. While studies have been conducted to monitor the movement, height, and melt rate of icebergs using SAR data, field studies, including laser ranging, acoustic imaging [19], global positioning systems(GPS), and buoys deployed on icebergs [20,21], it lacks in accounting for the random behavior of SAR data. Dynamic modeling of iceberg tracking requires specific inputs, such as iceberg topography, sea ice extent, ocean current, and wind speed.

The main objective of this study is to track the trajectory of iceberg A68 from July 2017 to February 2021 and analyze the iceberg area changes, change in the heading, and drift distance changes during approximately 3.5 years from its growth in July 2017 until it shattered into countless smaller pieces in February 2021. C-band SAR data of Sentinel-1 A and B spaceborne sensors were used to fulfill the study's goal. Ground range detected format medium resolution (GRDM) data from the spaceborne Sentinel 1A/B SAR sensor, a pre-focused, multi-looking, and ground range projected product, have been used to track A68. A detailed workflow of SAR data processing for iceberg tracking, and detection of the changes in the area, heading, and drift distance is given in Section 2.

Spaceborne Observation and Iceberg Detection

Satellite microwave scatterometers can watch Antarctica regularly, however, their poor spatial resolution makes them ineffective for iceberg detection and monitoring. Frost et al. investigated the use of a constant false alarm rate (CFAR) detector for detecting icebergs in infested areas, a technique typically used for ship detection [22]. The CFAR technique employs the use of adaptive statistical modeling to determine a detection threshold based on background clutter noise [23]. The sliding window technique is often implemented in tandem with CFAR, with the parameters for the hypothesis falling under this local window. Even then, with a homogeneous background, the hypothetical model does become contaminated by nearby targets, making it extremely sensitive to minor anomalies [24]. High iceberg density areas are one such common contamination source with the statistical modeling resulting in a combination of sea ice and icebergs instead of sea ice alone [22]. This is called the capture effect in the literature with serious degradation in CFAR detector performance [24–26]. Small islands, shoals, rocks, and islets are all typical elements that trigger false alarms in traditional detectors. Thus it becomes imperative to mask out land areas in the initial stage of processing [27]. The CFAR detector should be selected for the identification of bright objects that contribute to high scattering in comparison to cluttered sea background, as long as the adaptive window used is larger than these targets. During the winter months, the iceberg becomes encased in sea ice, posing a challenge.

SAR sensors are significantly more advantageous in that they can provide data in almost all climatic situations, except for the strongest rains, and are thus increasingly being employed for iceberg identification [28–32]. The radar backscatter intensity of icebergs is typically higher than that of their surroundings. The attenuation depth of the radar signal in the C-band ranges from 1 to 14 m in non-saline ice, with extra scattering caused by air pockets and contaminants within the iceberg [32–34]. As a result, both volume and surface scattering affect an iceberg's backscatter. Icebergs have a backscatter intensity of −6 dB to

−4 dB, sometimes greater [32], but the surrounding mixture of open ocean and sea ice has a backscatter intensity of less than −10 dB [28]. As a result, the lowest limit for the average backscatter coefficient has been established at −10 dB, which was obtained empirically.

Icebergs can put offshore oil, maritime, and gas production facilities, as well as subsea pipelines, in grave danger. Because of its cloud penetrative and night monitoring capabilities, SAR has a well-deserved reputation for remote sensing in polar areas. Figure 1 illustrates the interaction of electromagnetic waves and radar scattering from icebergs, surrounding sea ice, and the ocean. While single-channel SAR images have been used for iceberg detection and characterization in many studies [29,35–37], the dual- and quad-polarized data provided by RADARSAT-2 and Sentinel-1 respectively provide supplementary details obtained through multipolarization. This results in enhanced detection, classification, and characterization [38–40].

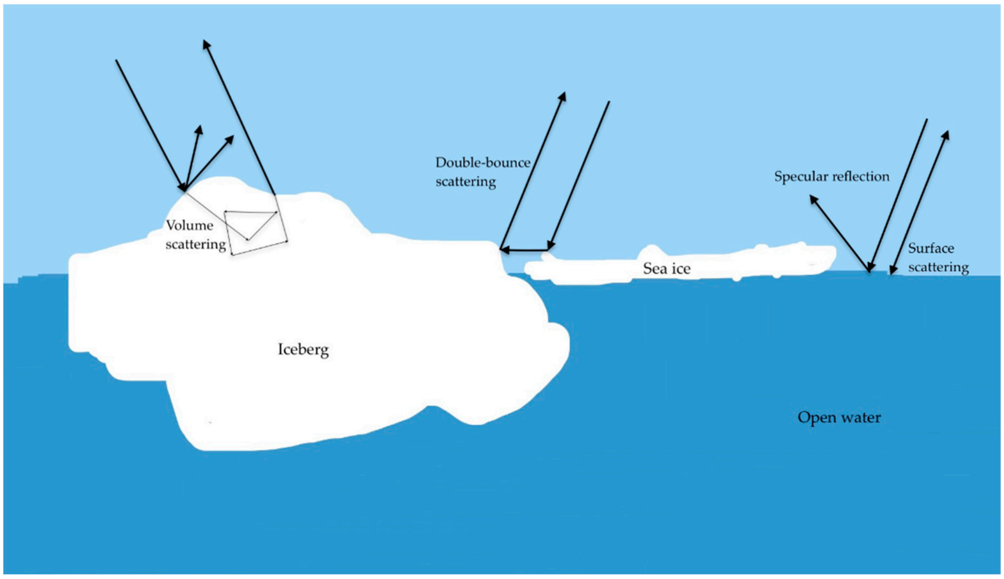

Figure 1. Microwave scattering mechanism from the iceberg, sea ice, and open water [35]. The black arrows depict the types of reflections involved for an iceberg surrounded by sea ice and ocean.

Due to differences in dielectric and geometrical features of objects, polarimetric SAR offers a variation in radar backscatter between classes [41]. This feature can be used to distinguish between water and ice and possibly classify different forms of ice depending on the structure, roughness, and salinity. Because icebergs and sea ice have distinct qualities and characteristics, it is necessary to distinguish the two [30]. As a result, icebergs are appearing brighter than sea ice. Furthermore, due to the large radar signal difference between the iceberg and background clutter in cold weather and calm open waters or recently produced unconstrained sea ice, icebergs are predisposed to easy identification.

2. Materials and Methods

In 2014, a fissure that had been present for nearly a decade began to propagate near the Gipps Ice Rise on the Larsen C ice shelf (LCIS), the Antarctic Peninsula's largest ice shelf. It resulted in the development of the huge tabular iceberg A68 in July 2017 after combining with other fissures northward. The Sentinel-1A SAR image of the study area is shown in Figure 2. When it first formed, it was 160 km long and 50 km wide, but it quickly broke into two sections, A68A and A68B. With a surface area of 90 km^2, A68B is the smaller of the two.

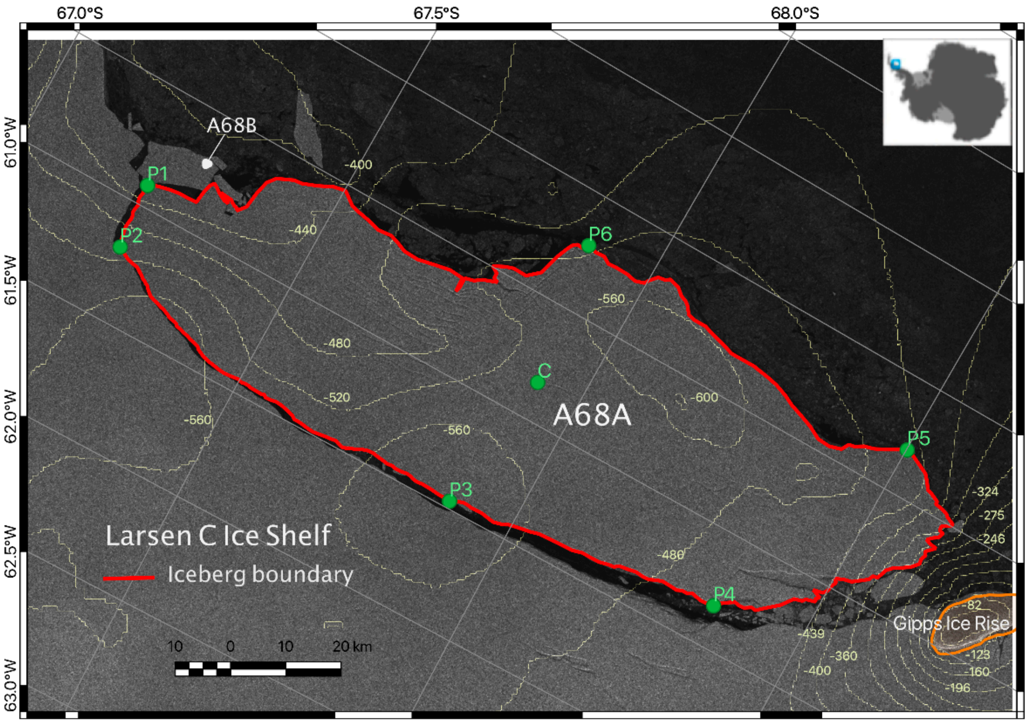

Figure 2. The contour of the seabed from the international bathymetric chart of the Southern Ocean (IBCSO) in the Antarctic polar stereographic projection overlaid with a Sentinel−1A synthetic aperture radar (SAR) picture for the study region (rectangle in the inset) taken on 27 July 2017. On the iceberg's edges, points P2, P3, P4, P5, and P6 have barely displayed any calving. At sites P1, C, and P7, the iceberg's distance traveled and heading (rotation) were computed.

The Larsen C Ice Shelf, which is in the northwest part of the Weddell Sea, is one of a sequence of Larsen ice shelves that run along the Antarctic Peninsula's northeast edge. It is separated from South America's southernmost point by the highly notorious Drake Passage which is nearly 1000 km away from it. The peninsula enjoys the mildest climate on the continent because it is the northernmost section of Antarctica and lies above the Antarctic Circle. Its hottest month is January, with temperatures averaging 1 to 2 °C, and its coldest month is June, with temperatures averaging 15 to 20 °C. The Antarctic Peninsula has been under scrutiny in the past decades for the observed intense warming the region has experienced due to climate change.

The flat plateau top is a common feature of tabular icebergs calved from Antarctica's ice sheets. The thickness of the iceberg A68 was posited to be ~300 m weighing over a trillion tons [42]. It is the largest iceberg on satellite records currently and is expected to take years, if not decades to fully calve or disintegrate.

2.1. *Collapse of the Larsen C Ice Shelf and Evolution of Iceberg A68*

Some of the prominent ice shelves in Antarctica are the Ross Ice Shelf (472,960 km^2), the Ronne–Filchner Ice Shelf (422,440 km^2), the Amery Ice Shelf (62,620 km^2), and the Larsen C Ice Shelf (48,000 km^2) [43]. Ice shelves are formed when a huge mass of ice advances slowly in the forms of glaciers and ice streams from ice sheets into the surrounding sea. The low temperature of the surrounding ocean does not allow this ice to melt right away. This in turn floats on the surface (since ice is less dense than water) and grows larger by amassing more ice from the glacial flow. This mass may survive thousands of years owing to grounding by islands, ice rises, and rock peninsulas. Ice shelves continuously grow by ice from land and lose mass by calving events. This maintains dynamic stability. Since ice shelves already float in the ocean, it is incorrect to say they contribute directly to sea-level rise. The collapse of an ice shelf gives way to an enhanced surge in glaciers and ice streams that feed into it by decreasing the buttressing effect provided by ice shelves to inland glaciers and ice streams. Since glaciers and ice streams are on land, their movement into the ocean contributes to sea-level rise. Hence ice shelf collapse does contribute to sea level rise, albeit indirectly. Recent research suggests ice shelf collapse may enhance glacial flow by two to six times [44].

An unusual sequence of ice shelf collapses has been observed by scientists in Antarctica and the Arctic in the last 30 years. Although iceberg formation through calving events is not unusual, the process normally takes place over months and years as rifts form on the ice shelf. It is, however, unusual for the process to happen over a few days, as observed in the Wilkins Ice Shelf retreat in Antarctica in 2008 or the ice shelves along Ellesmere Island in Northern Canada [45]. On the contrary, the collapses in previous instances spanned over weeks, leaving a spew of chunky icebergs, small and large. The remaining ice shelves retreated by as much as 90 percent, with several experiencing recent collapses. Most of the fast-retreating ice shelves are located in the Antarctic Peninsula. Rapid ice shelf collapse has been attributed to warmer air and water temperatures and meltwater formation on the ice shelf surface. Ponds of meltwater are formed over the surface of the ice shelf as warm air melts it. This water seeps through the cracks on the surface and travels deeper, eroding and expanding those cracks [46]. From the underside, warm water melts the ice shelf surface from below, causing it to thin, and leaving it susceptible to cracking [47]. Recent research has also suggested the waning of sea ice surrounding ice shelves as a contributing factor to ice shelf disintegration, as it provides a protective layer between the ice shelf and the encompassing ocean, serving as a buffer between ocean swells and storms. The increased seasonal absence of sea ice may be a commonly overlooked causal factor when accounting for ice shelf collapse. Wave-induced flection may trigger outer margin fracturing and calving events [48]. Ice shelves serve as an important buffer between grounded Antarctic ice and sea, hence it is imperative to determine their long-term stability to better model Antarctic mass balance and climate feedback models.

By mid-2016, iceberg A68 had begun to calve [49]. Scientists noticed a widening rift running along the Larsen C Ice Shelf on 10 November 2016 [50], which ran 110 km long and 91 m wide, and a depth of 500 m. Subsequent sporadic rift propagation led to its formation on 12 July 2017, resulting in the largest iceberg on current remote sensing records, measuring an area of about 5800 km^2. It represented nearly 12% of the entire LCIS area. Such calving events could precondition ice shelves for instability, as observed for the Larsen B Ice Shelf in January 1985, when a gigantic iceberg calved, leaving the ice shelf in retreat until it collapsed completely in 1992. Ice sheet models, such as BAS-APISM and BISICLES [51], when applied to the Larsen C and George VI ice shelves demonstrate a considerable role of existing basal/surface crevasses on the stability of the remaining ice shelves. The calving of A68 should remove back stress at the new calving front and increase extensional longitudinal stress. Such an event would place additional stress on existing flow-transverse crevasses, consequently leading to increased calving rates and potential instability [52].

2.2. Dataset

From 28 June 2017, until 29 January 2021, 47 Sentinel-1 SAR images were selected for this study, which were utilized to estimate the area and drift. Table A1 in Appendix A provides the specifics for each dataset. The images were obtained via the Data Search Vertex portal of the Alaska Satellite Facility.

2.3. SAR Data Preprocessing Workflow

A blanket workflow was employed to preprocess all of the acquired scenes of the SAR data. The data processing was performed with The Sentinel-1 Toolbox (S1TBX) of the Sentinel Application Platform (SNAP). The SAR data processing flow diagram is shown in Figure 3.

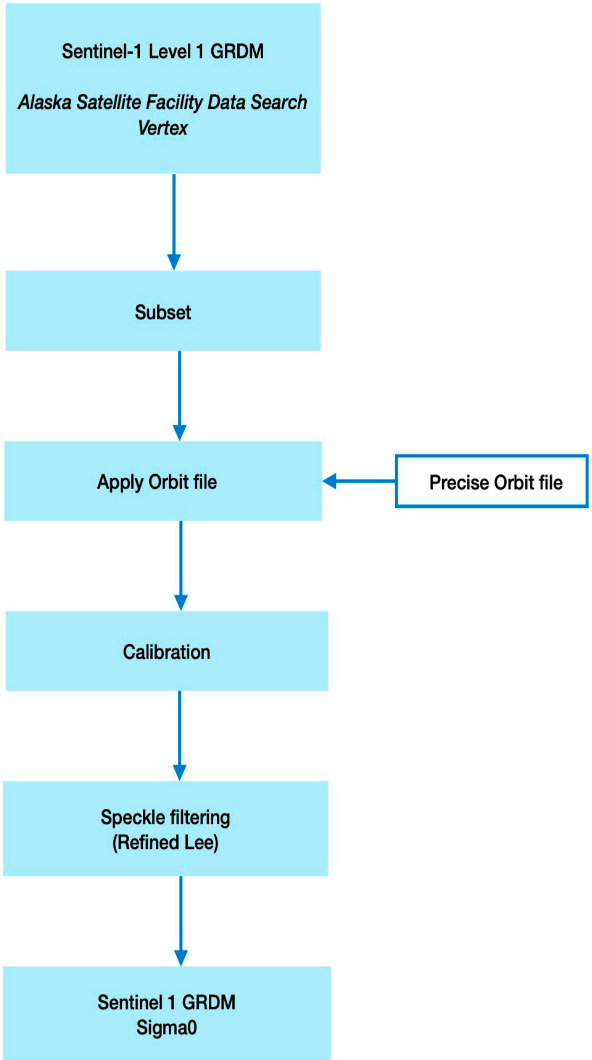

Figure 3. Batch processing workflow for all scenes in the time series.

The scenes were spatially subset to include the area under study, to reduce processing time for subsequent steps. The orbit correction of the Sentinel-1 data was performed with the precise orbit files. The orbit-corrected data were radiometrically calibrated to measure the radar backscatter of the SAR resolution cells. Speckle filtering was performed to minimize the speckle noise from the SAR data.

2.4. Trajectory Analysis

2.4.1. Ellipsoid Correction

Range Doppler ellipsoid correction was performed for all of the acquired scenes. Since sea surface undulations are not of paramount importance for the study area, the average height range Doppler ellipsoid correction was preferred on all 47 scenes of the Sentinel-1 data. This also reduces the computational time required for the processing. A predefined map projection, the EPSG:3031 WGS 84/Antarctic polar stereographic was employed for accurate visualization and subsequent area and drift analysis. The datum used was the World Geodetic System (WGS) 1984.

2.4.2. Area Calculation

The ellipsoid-corrected data were then converted into the GeoTiff format, which is readable by GIS software, such as QGIS. This was carried out to facilitate area calculation and for studying the effects of sea-bed topography and ice rises on the target's evolution.

The images were superimposed to study the trajectory followed by iceberg A68 and note the gradual advancement of A68 to the Southern Ocean. A vector data container (mask) was created manually by delineating the detached iceberg. The mask area was computed using the mean Earth radius of 6378.137 km. A Cartesian calculation system was used for the computation of the area and perimeter since the raster had already been reprojected to the Antarctica polar stereographic projection. Contour tracing was carried out manually for all scenes multiple times to account for manual errors while delineating, and the standard deviation was calculated. A total of 47 images were manually delineated monthly from July 2017 to February 2021.

2.4.3. Analysis of Bathymetry on A68's Evolution

To investigate the influence of sea bed topography on A68's evolution, the international bathymetric chart of the Southern Ocean (IBCSO) was used as an overlay on the study area. The IBCSO is a seamless bathymetric grid of the Southern Ocean that compiles all available data from several international sources to cover the whole Antarctic Treaty Area south of 60° S. The IBCSO v1.0 grid is based on a polar stereographic projection at 65° S on the WGS-84 ellipsoid [53] and has a resolution of 500 m × 500 m. Quantarctica 3 from the Norwegian Polar Institute was used to access the grid. The IBCSO database includes over 4200 million ocean scenes from a variety of sources throughout the world. Multibeam surveys account for 98 percent of the data, while single beam surveys, digital nautical charts, and other datasets account for the remaining 2%. For the topography of continental Antarctica and sub-ice-shelf bathymetry, Bedmap2's subglacial bed elevation layer was used. The information was verified, homogenized, and saved in a standard data format. In an iterative procedure, the final bathymetric model was gridded and cleaned [53]. Each scene was overlaid with an IBCSO chart, and the influence of the seafloor elevation was investigated for each image.

3. Results and Discussion

A short time after A68 calved from the Larsen C Ice Shelf, a small chunk broke away from it, known as A68B. Measuring 90 km^2, it accounted for nearly 2% of A68's entire area. The remaining larger portion left was labeled as A68A which is the main focus of this study.

3.1. A68 Area

The area changes of iceberg A68A were derived by repeated manual contour tracing from Sentinel-1 data. The repetitions were carried out to account for manual errors while delineating, and the standard deviation was calculated for every month since July 2017. The calculated area is based on Cartesian calculation. The changes were observed monthly until May 2020, with a total of 36 scenes used for the analysis. The final calving of A68 occurred on 12 July 2017, with its area measuring 5758.359 km^2 on 27 July 2017. The major and minor axis, as shown, were calculated to be 157.01 km and 51.38 km, respectively (Figure 4). Over the next two months, it saw a slight decrease in the area with its area standing at 5648.56 km^2 in August 2017 and 5606.2 km^2 in September. This could be due to some chunks of ice breaking away from the northern portion of A68A when it moved toward the LCIS (Figure 5a,b). It then saw a minor increase in area to 5620.6 km^2 and 5636.3 km^2 in October and November, respectively. December 2017 saw a slight decrease in the area to 5592.76 km^2. In December 2017 and January 2018, the northern part of the iceberg (P1 and P2) was low in brightness level, presumably due to the austral summer (Figure 5e,f).

January 2018 again saw a decrease in the area by almost 30 km^2 with an increase of 60 km^2 in February 2018. It then saw a steady decrease by an average of 40 km^2 per month until July 2018, mostly due to a steady stream of breakage from the northern corner of the iceberg, with chunks observable in April (complete calving of P1, now marked as P1′), May, and June 2018 (Figure 6c–e). Post that, the area remained almost constant at an average of 5491.25 km^2. November 2018 saw a slight increase in area by 16 km^2 which can be attributed to digitization error by manual delineation or actual longitudinal stretching of the iceberg. The standard deviation calculated to account for digitizing errors through repeated contour tracing ranged from 3.2 to 6.4 km^2. Furthermore, the variations in the iceberg area did not match the trends in air temperature indicated by MERRA-2 reanalysis data [18], hence the parameter was not included in this study and only bathymetry was focused upon to have a deeper understanding of complex coastal geometry in the iceberg's early evolution.

A68A's area continued to decrease until the beginning of 2019 by an average of 62.5 km^2/month. In January 2019, the southern part of A68A appeared to return low backscatter, due to surface melting in summer. This made manual contour tracking challenging and could be the cause of some discrepancies in area calculation (Figure 7f). In February 2019, an ice chunk calved off from the northeast side of the iceberg measuring 65.5 km^2 (Figure 8a). The area continued to decline with an average of 19.25 km^2 per month until July when it saw a slight increase by 24 km^2. This is owing to the iceberg's longitudinal stretching caused by the decline in surrounding sea ice, which acts as a pseudo-restraining force [54,55]. This is quite similar to how icebergs exert a buttressing force on ice shelves, and the calving of which may cause ice shelves' thinning or longitudinal stretching [56].

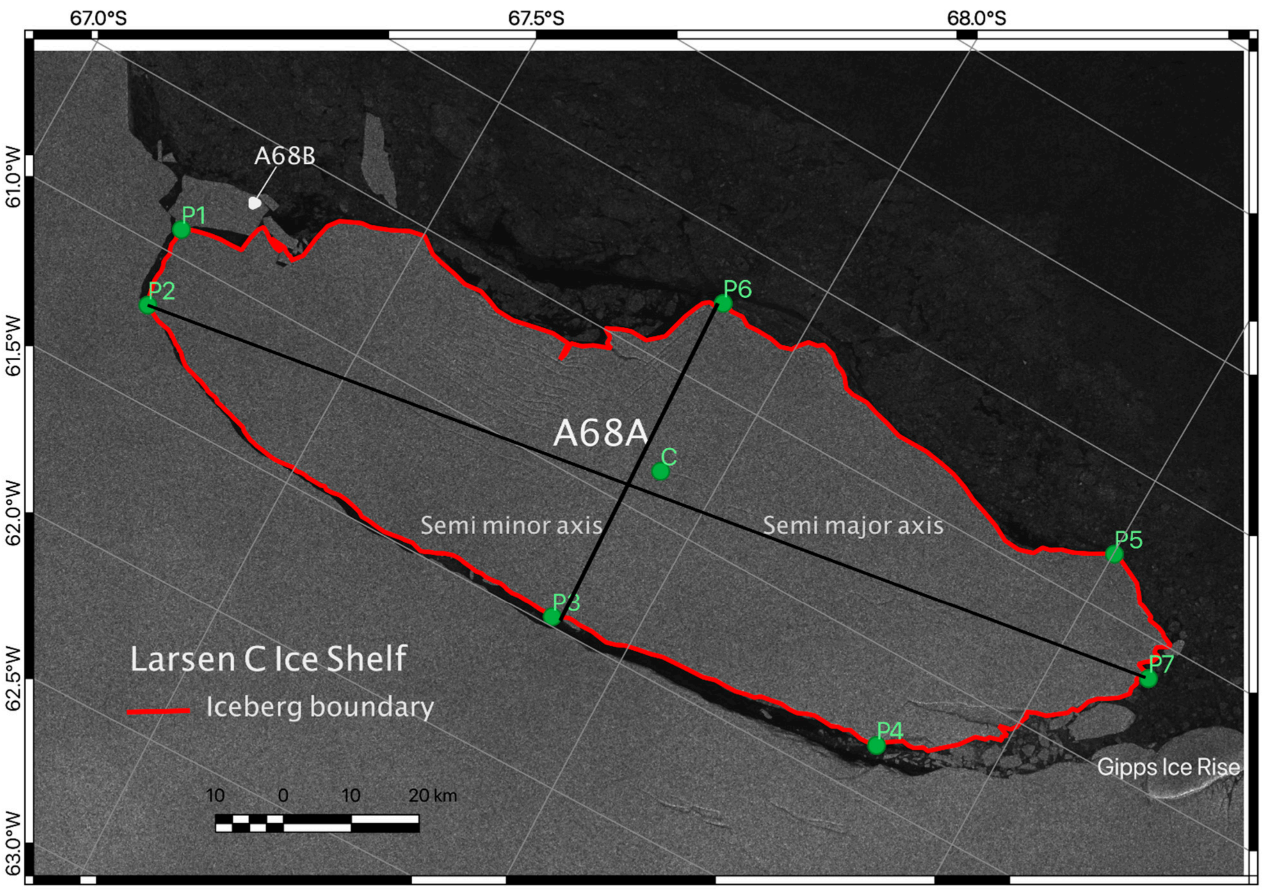

Figure 4. Depiction of the semi-major and semi-minor axis a few days after A68's formation (27 July 2017).

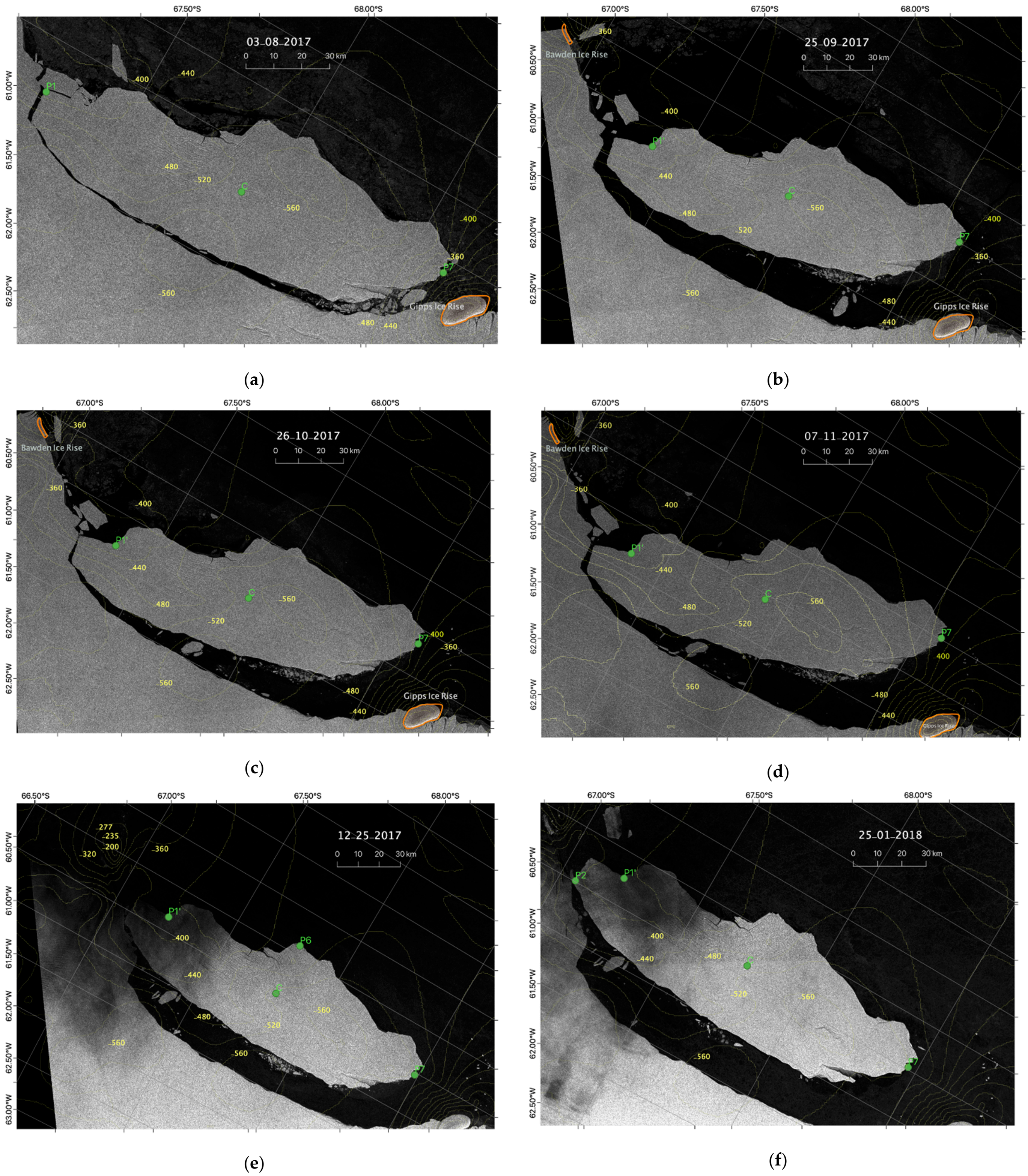

Figure 5. Sentinel-1 SAR images of iceberg A68A were acquired on (**a**) 3 August 2017; (**b**) 25 September 2017; (**c**) 26 October 2017; (**d**) 7 November 2017; (**e**) 25 December 2017; and (**f**) 25 January 2018.

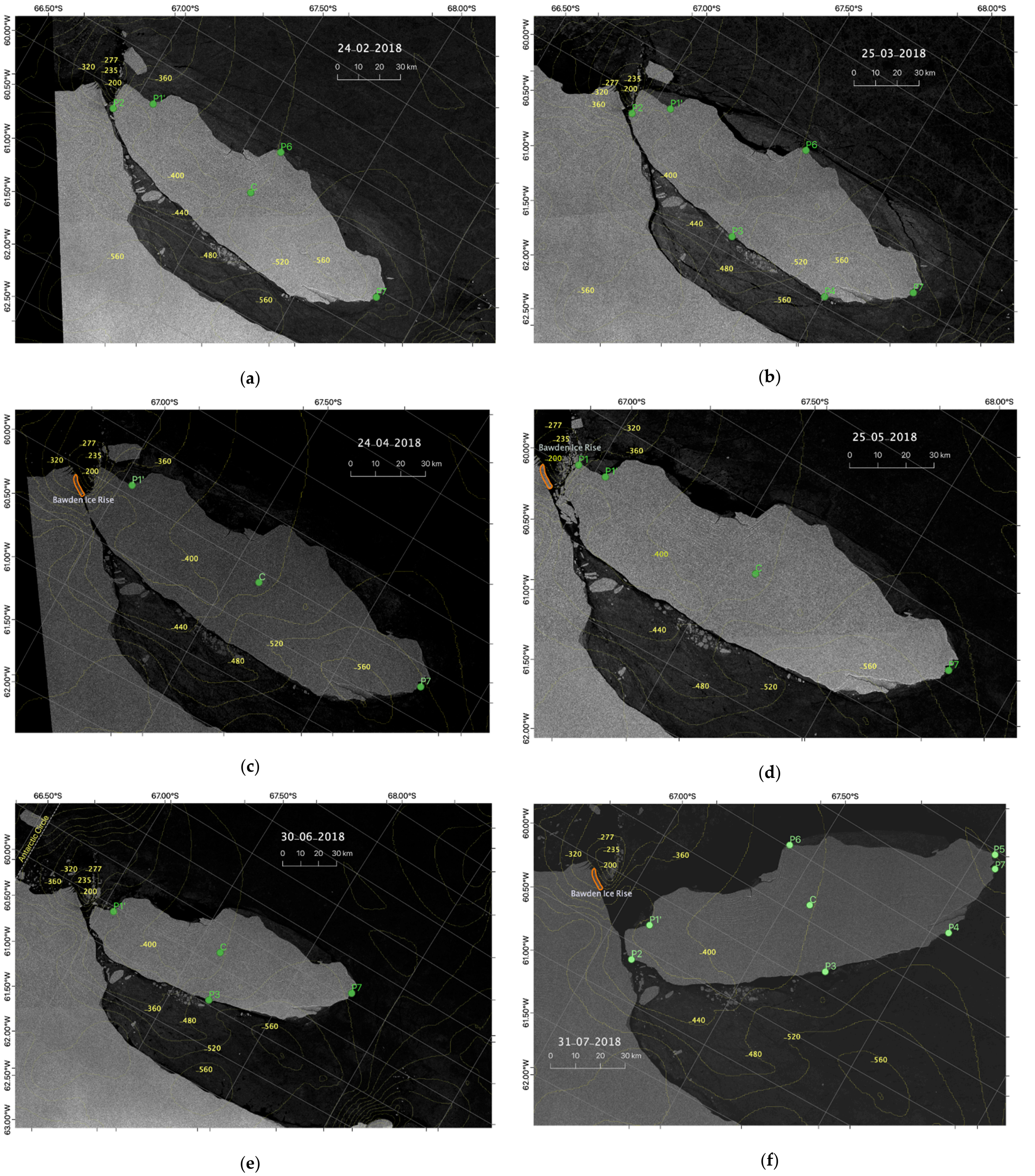

Figure 6. Sentinel-1 SAR images of iceberg A68A for (**a**) 24 February 2018; (**b**) 25 March 2018; (**c**) 24 April 2018; (**d**) 25 May 2018; (**e**) 30 June 2018; and (**f**) 31 July 2018.

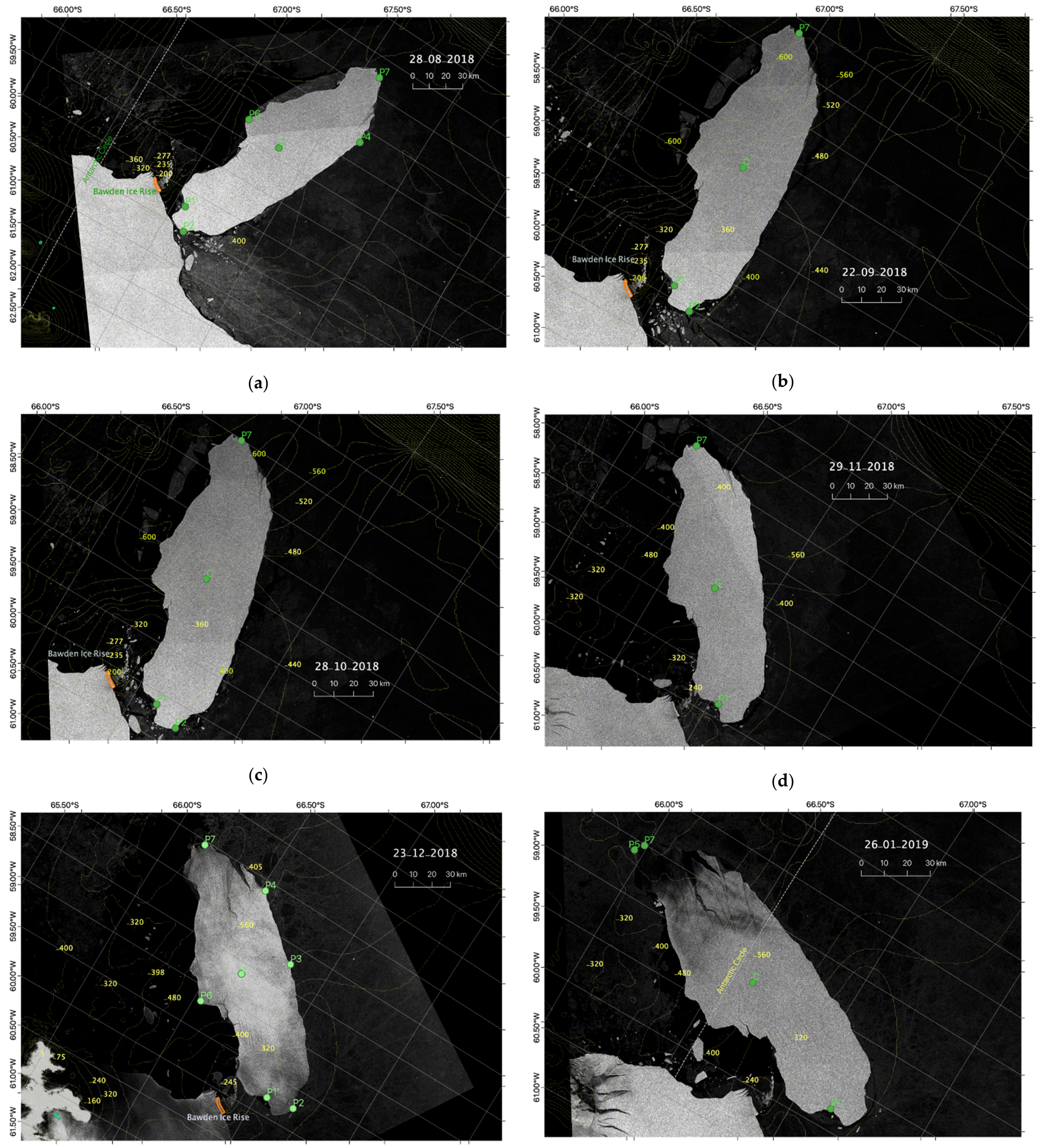

(**a**) (**b**)

(**c**) (**d**)

(**e**) (**f**)

Figure 7. Sentinel-1 SAR images of iceberg A68A for (**a**) 28 August 2018; (**b**) 22 September 2018; (**c**) 28 October 2018; (**d**) 29 November 2018; (**e**) 23 December 2018; and (**f**) 26 January 2019.

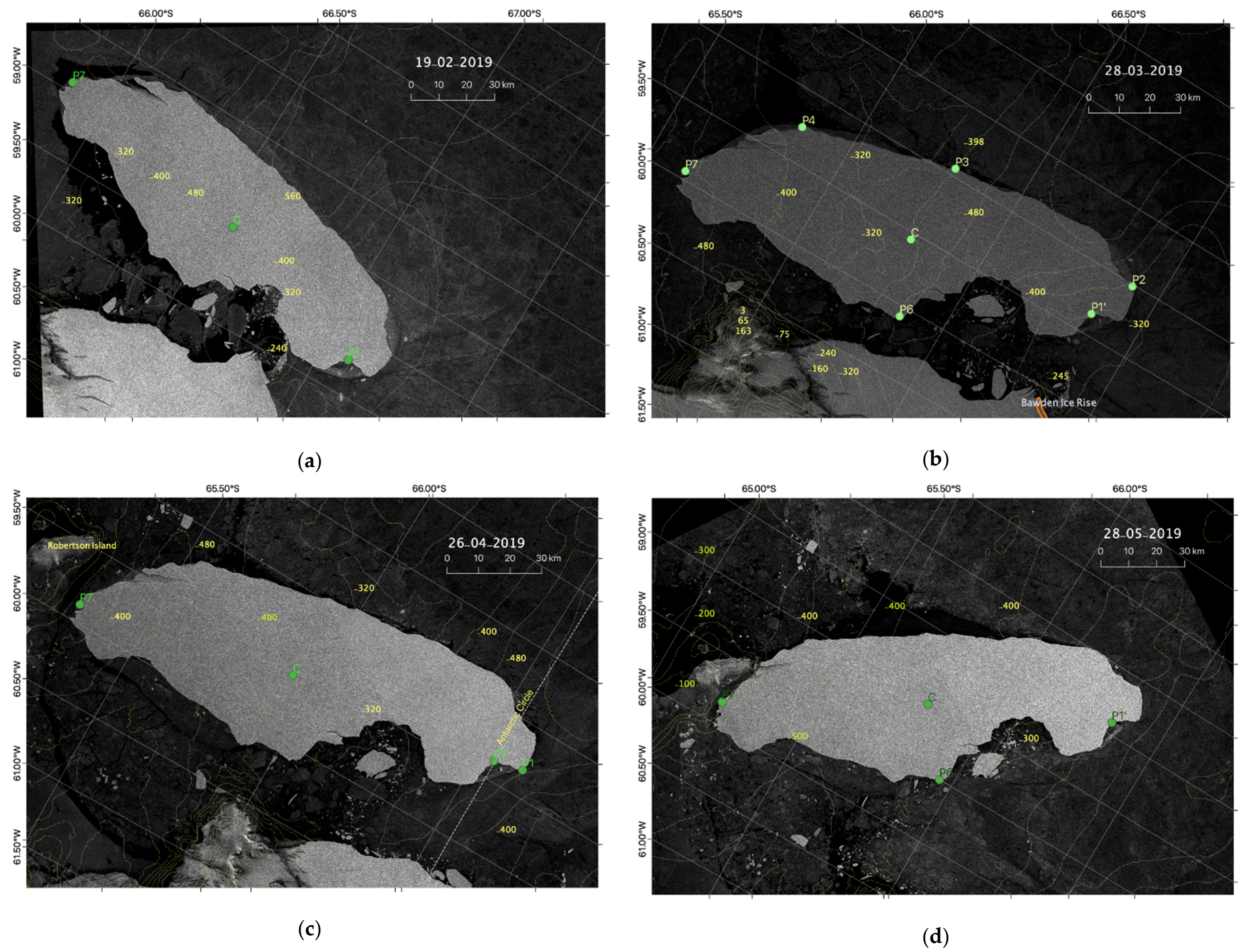

Figure 8. Sentinel-1 SAR images of iceberg A68A for (**a**) 19 February 2019; (**b**) 28 March 2019; (**c**) 26 April 2019; and (**d**) 28 May 2019.

From August 2019 (Figure 9c) to November 2019 (Figure 9f), there anywhere no sudden changes in the area until December 2019, with a decrease of almost 65 km^2. This also marked the onset of peak austral summer, which can be corroborated by the darkening of almost the entire iceberg (Figure 10) in likeness to the surrounding sea ice. This may be either due to snowfall or surface melt on the iceberg, resulting in specular reflection. By this time, the iceberg had reached the edge of the Antarctic Peninsula and was almost headed into open waters in the South Atlantic Ocean.

Even though the backscatter from A68 had decreased, it brought an unexpected advantage with it. A few fissure-like markings running along the length of the iceberg were visible in sharp contrast (Figure 10a). Future studies can analyze the role of these markings and whether they play a role in further disintegration of the iceberg. Most of these markings ran longitudinally on the surface of the iceberg and were visible only during some scenes. It should be pointed here that in the image from January 2020, the iceberg appears completely blacked out due to specular reflection. The above-mentioned markings are not visible as sharply in this scene, possibly due to enhanced melting on the iceberg's surface (Figure 10b). Furthermore, it is worth noting the comparative high backscatter signal from the ocean swell and/or sea ice during these two months. The backscatter amount received in February 2020 (Figure 10c) is less than the SAR backscatter in March 2020 (Figure 10d). April 2020 marked yet another calving event from the eastern side of the iceberg, above P6 (Figure 10e). Standing at 155 km^2, this piece named A68C accounted for nearly 3.08% of the entire iceberg's surface area. As of May 2020, A68's area was 4618.417 km^2, which is 80.54% of the total area when it first formed back in July 2017.

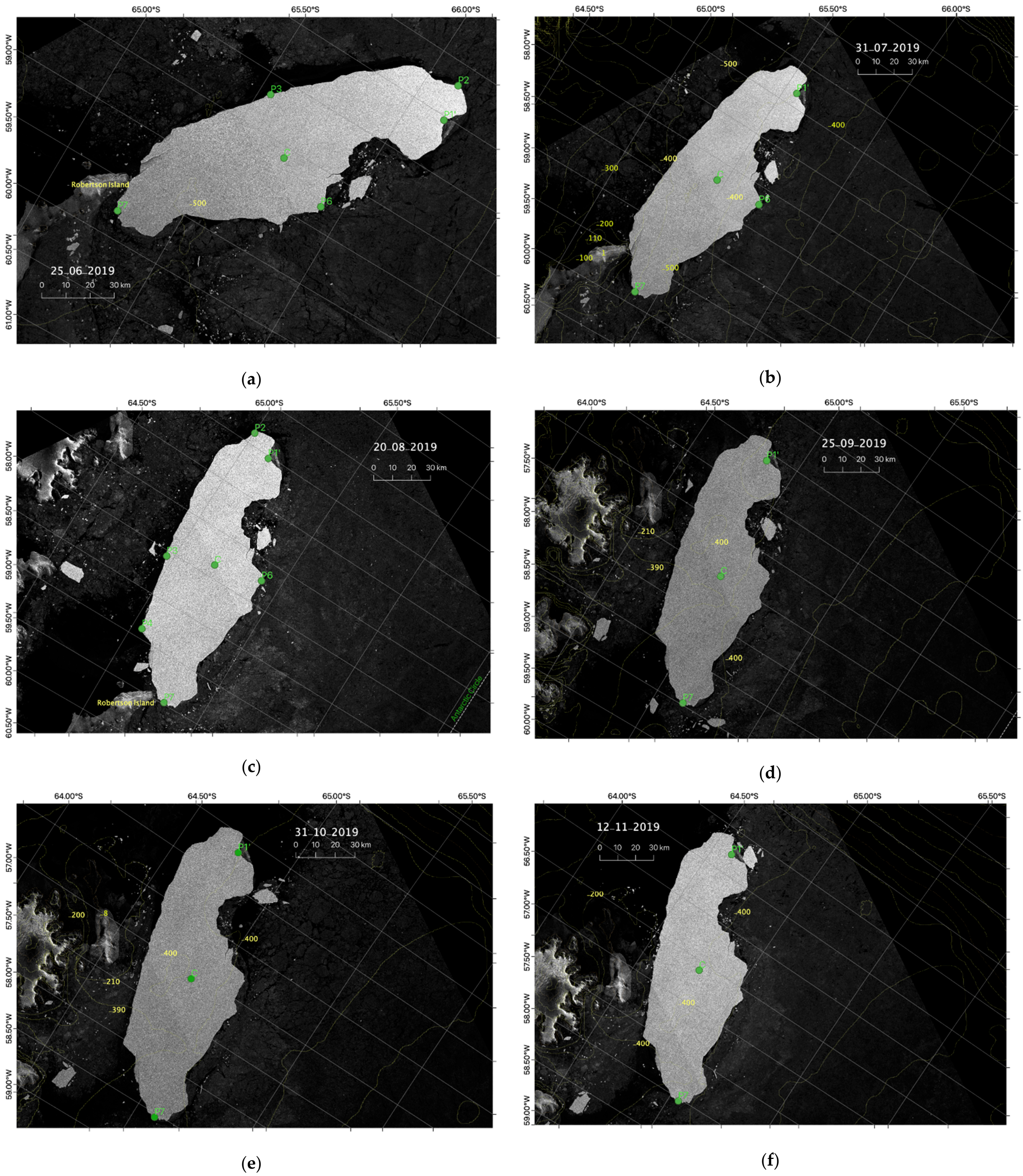

Figure 9. Sentinel-1 SAR images of iceberg A68A acquired on (**a**) 25 June 2019; (**b**) 31 July 2019; (**c**) 20 August 2019; (**d**) 25 September 2019; (**e**) 31 October 2019; and (**f**) 12 November 2019.

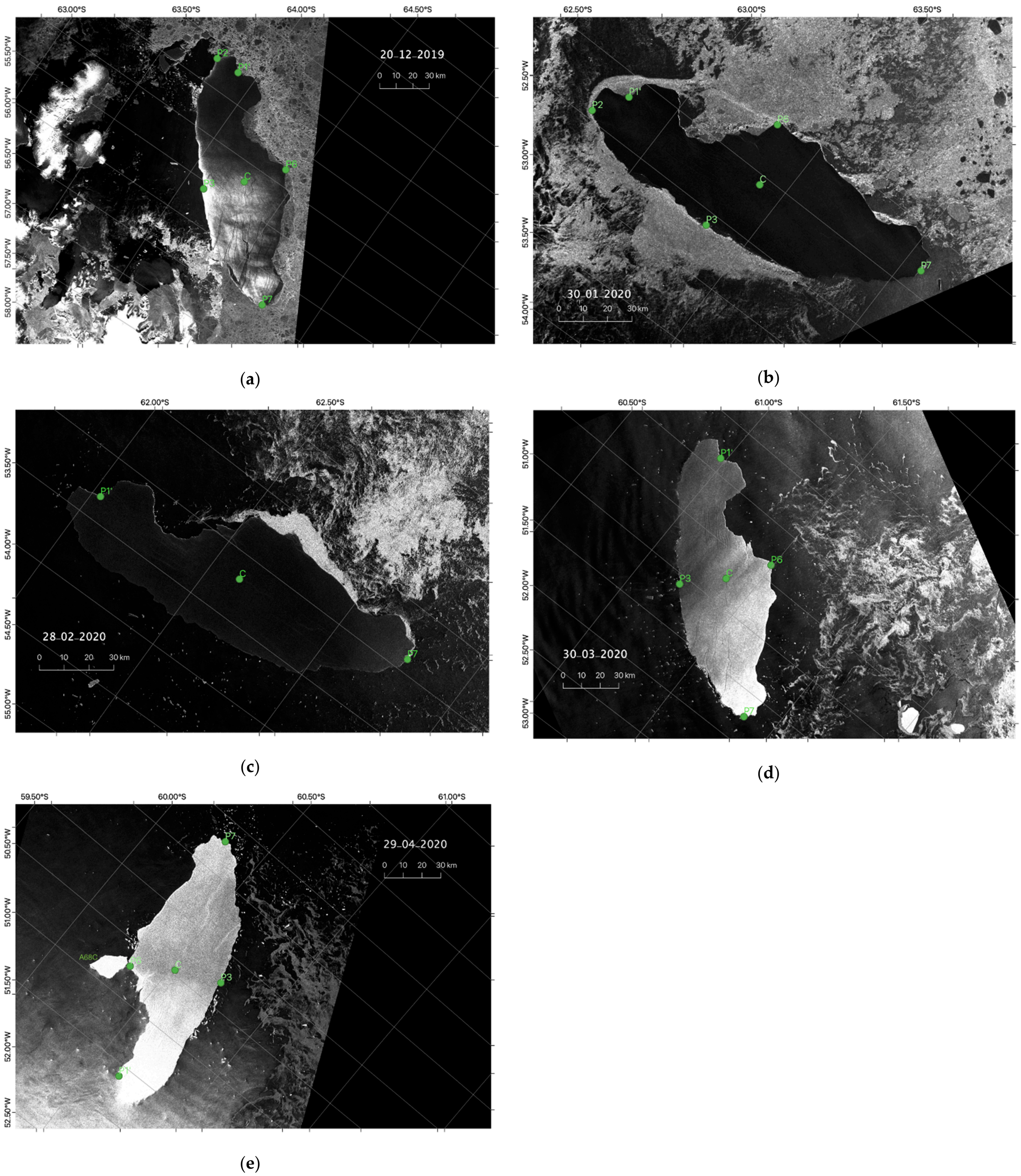

(**a**) (**b**) (**c**) (**d**) (**e**)

Figure 10. Sentinel-1 SAR image for (**a**) 20 December 2019. Notice the enhanced longitudinal markings in the southern portion of the iceberg. Future calving might give an insight into the role of these seemingly fissure-like features in iceberg calving and disintegration processes. (**b**) 30 January 2020; (**c**) 28 February 2020; (**d**) 30 March 2020; and (**e**) 29 April 2020 showing the newly formed A68C ice fragments around A68A.

From May 2020 to October 2020, the decrease in the area was a modest 63.6 km^2/month. September through November showed signs of steadily increasing surface melting due to the progressive darkening of the iceberg, owing to decreased backscatter (Figure 11d–f). 22 December 2020 marked a massive calving event near P1, as shown in Figure 12a, giving rise to A68D (16.7 km × 7.8 km), A68E (58.81 km × 12.2 km), and A68F (14.3 km × 11.34 km) measuring 146.19 km^2, 218.846 km^2, and 650.424 km^2, respectively. The shallow bathymetry near the islands is posited to have played a crucial role in aiding the fragmentation of A68. At this point, A68A (67.77 km × 39.72 km) stood at 2600.05 km^2, 45.15% of its original area when it calved from Larsen C.

January 2021 continued with debris from these smaller fragments breaking away, as can be seen in the backscatter from the sea surrounding A68D and A68E (Figure 12b). Twenty-nine January, 2021 saw another calving occurrence (Figure 12c) with the formation of A68G (51 km × 16.77 km) and A68H (18.78 km × 8.3 km) standing at 671.86 km^2 and 134.2 km^2, respectively, leaving the largest piece A68A (64.23 km × 22.34 km) at 1365.42 km^2, 23.71% of its original dimension.

The warm water of the Southern Ocean coupled with the shallow seabed near South Georgia and South Sandwich Islands seem to have finally succeeded in bringing the chapter of A68's journey to its end with more fragmentation expected over the next couple of months.

It can be very easily observed from Figure 13 that the surface area of A68 has decreased over time with a major dip occurring after January 2020 through to the end of the year.

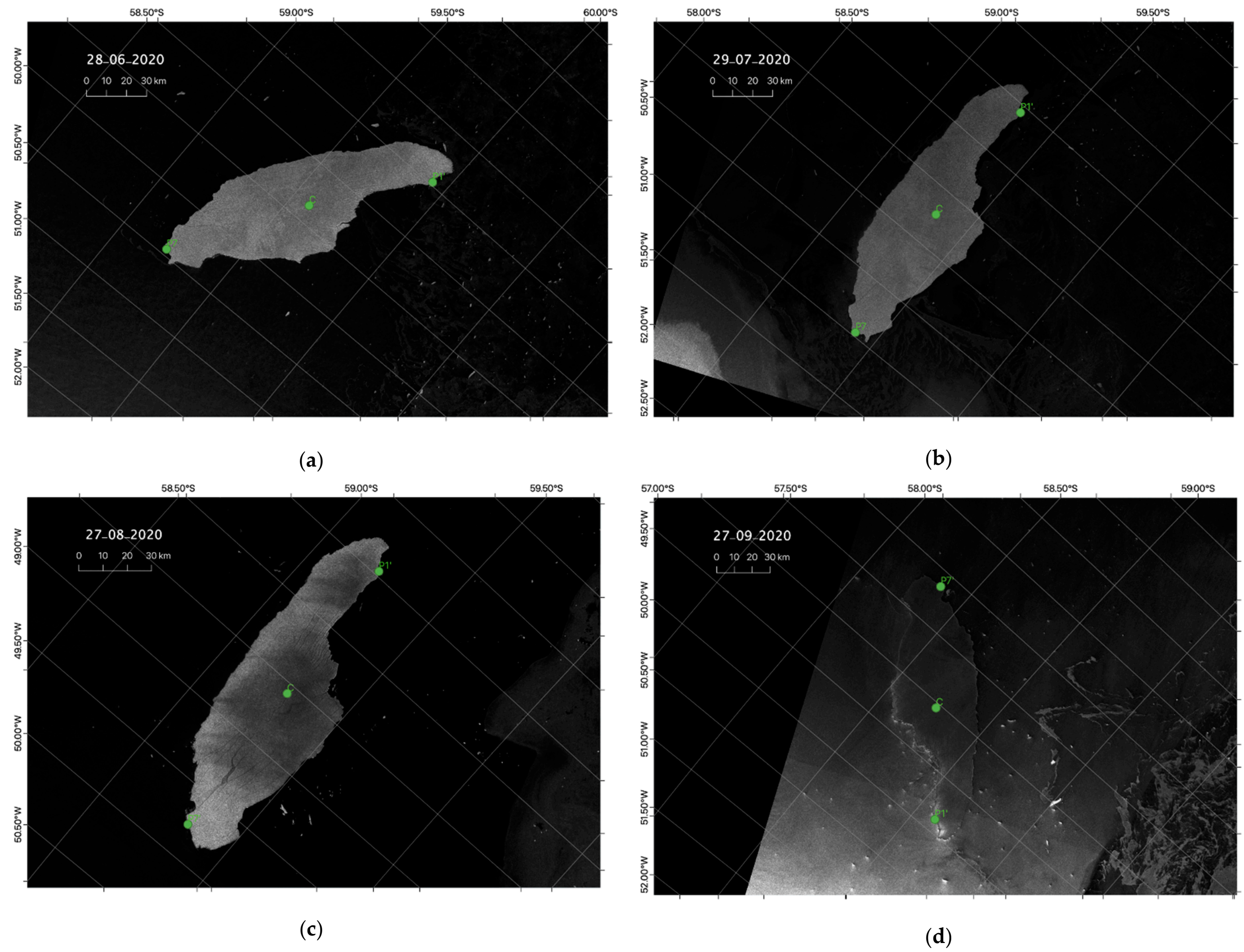

Figure 11. *Cont.*

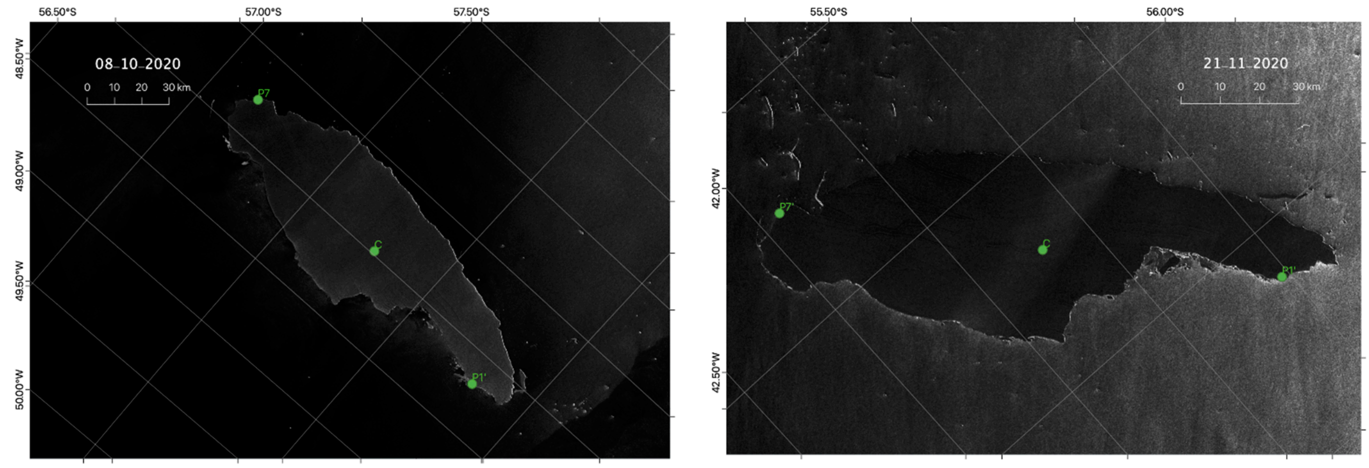

(**e**) (**f**)

Figure 11. Sentinel-1 SAR images of iceberg A68A for (**a**) 28 June 2020; (**b**) 29 July 2020; (**c**) 27 August 2020; (**d**) 27 September 2020; (**e**) 8 October 2020; and (**f**) 21 November 2020.

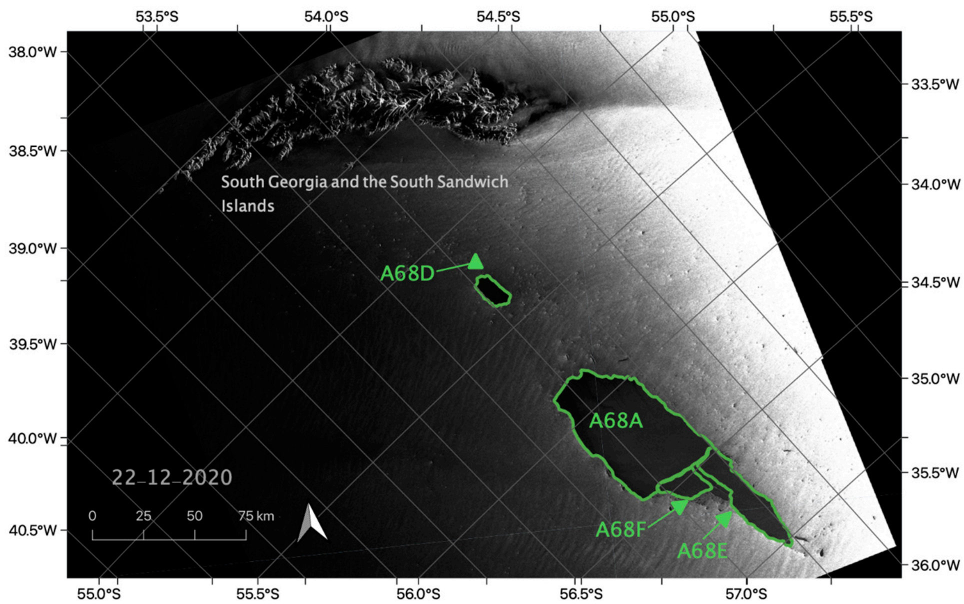

(**a**)

Figure 12. *Cont*.

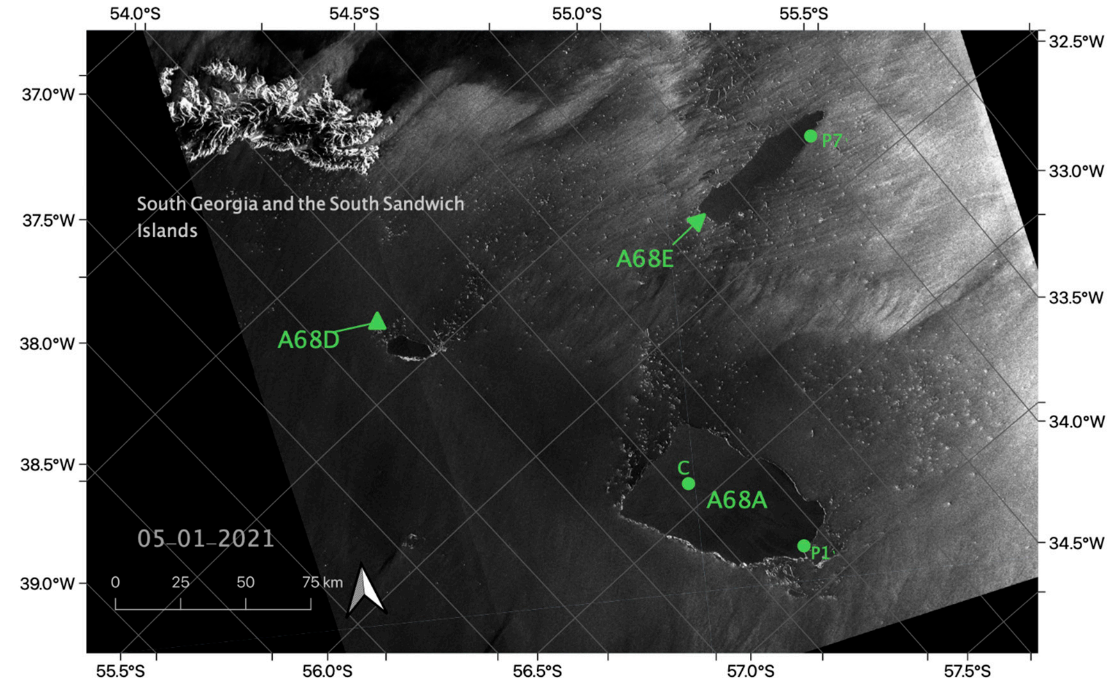

(**b**)

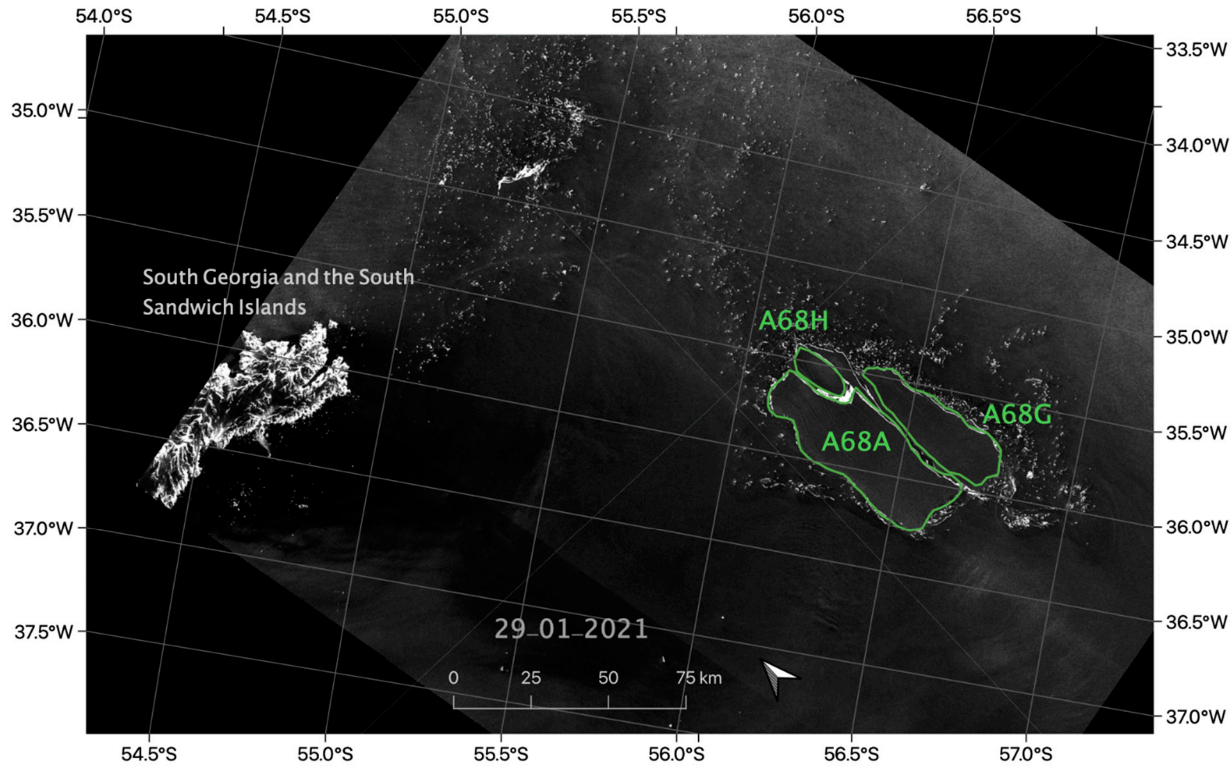

(**c**)

Figure 12. Sentinel-1 SAR image for (**a**) 22 December 2020 showing the calving of A68D, A68E, and A68F; (**b**) 5 January 2021 with A68E and A68D in the vicinity of A68A; and (**c**) 29 January 2021 with yet another calving of A68G and A68H.

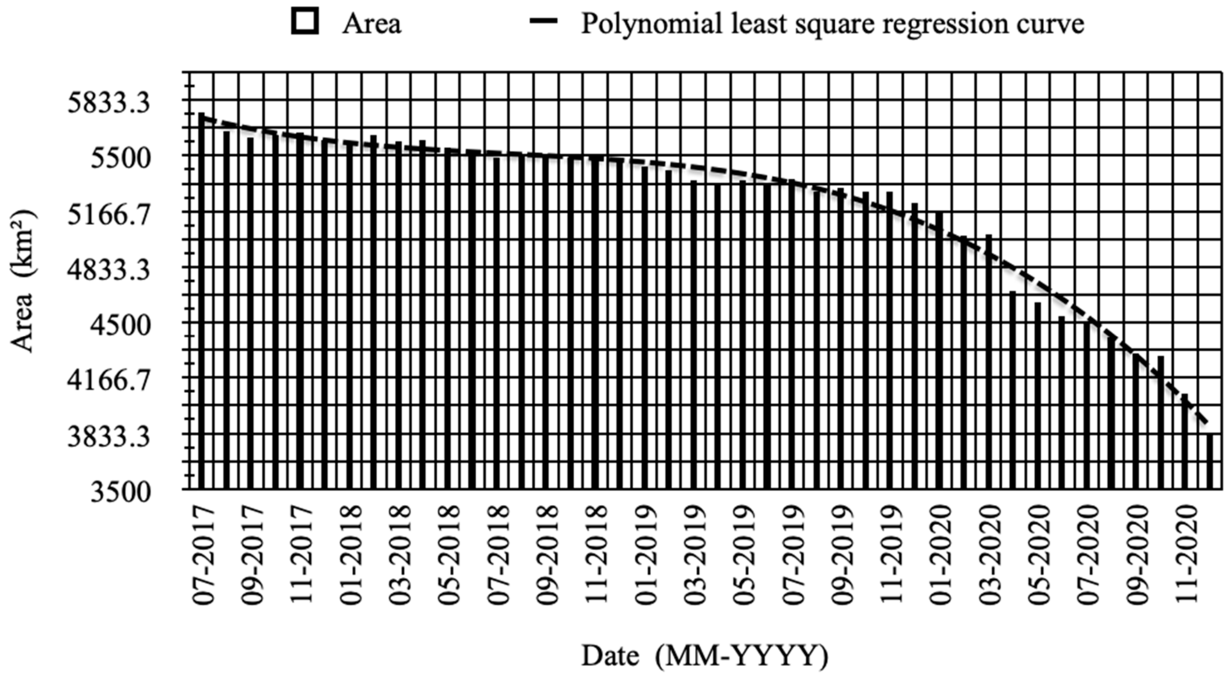

Figure 13. Changes in the area of iceberg A68.

3.2. A68 Trajectory

During its first month of formation after calving from the LCIS, A68A lay roughly on the coordinates mentioned below. Points P1, P2, P3, P4, P5, P6, and P7 have been marked in Figure 2 for better understanding. In August 2017, southerly winds with a speed of 6–12 m/s flew in the region [18] and can be assumed to be strong enough to move the southern part of the iceberg, i.e., P3, P4, P5 away from the LCIS. The chasm between A68A and the LCIS widened and this can be attributed to the strong southerly winds. This also enabled some large pieces of ice to calve from A68A and push it northward to break the surrounding sea ice (Figure 5a,b) [57]. From August 2017 to November 2017 (Figure 5a–d), A68A's southern portion continued to drift away in minor drags from the LCIS until December 2017 when the north portion (P1 and P2) also showed a noticeable shift away from the LCIS. At the end of December 2017, the major axis of the iceberg was more or less parallel to the LCIS portion from where it had detached (Figure 5e). However, it should be mentioned that the total shift in P1 and P2 towards the end of 2017 was minute and this may be attributed to collision with the shallow seabed of the Bawden Ice Rise at the northern edge. The Bawden Ice Rise, located near the northern edge of A68, is higher than −300 m. Some fragments from A68 were created presumably due to crack propagation on the top and bottom surfaces (Figure 6d).

The northward movement of A68A away from the LCIS continued somewhat uniformly throughout its entire length until May 2018. From June 2018 (Figure 6e), the southern portion of A68A (P4, P5, P7) started a counter-clockwise rotation about its centroid to break free from the LCIS. Up until July 2018, the drift speed at the center of the iceberg had been roughly 60 km/month, with the northern and southern ends of the iceberg showing a lower drift speed. This restriction can be attributed to the front of the Larsen C Ice Shelf and the thick sea ice surrounding it. The wind direction up to this point had been largely northwards with wind speeds of up to 4–7 m/s [18]. This enabled it to gently emerge from the LCIS in July 2018 (Figure 6f) with an almost circular motion. It was able to emerge completely from the A68 shaped bay in the LCIS with the northern part still pivoted near the Bawden Ice Rise. The shallow seabed near the Bawden Ice Rise likely played the main role in this rotation, as compared to the westerly winds that had become more predominant in that period. It must be mentioned here that only the northern portion (P1 and P2) remained held by the shallow seabed topography and the southern portion (P4, P5, and P7) rotated freely with the former acting as a fulcrum for the counter-clockwise drift of the latter. This rotation continued from August 2018 through September 2018 with the iceberg's center moving by almost 43.3 km in a month, by which point the northern part had also moved by 19.6 km away from the LCIS (Figure 7a,b). From September 2018 to February 2019 (Figure 7), the iceberg's center saw a complete rotation about its northern pivot with an average of 17.7 km/month drift (Figure 14a) and a 247.21 degrees rotation (Figure 14b). The fact that the iceberg's motion style changed dramatically in April 2019 is noteworthy in the iceberg's trajectory, the southern portion (P4, P5, P7) now became the pivot, with proximity to the LCIS and Bawden Ice rise and the northern portion moving counter-clockwise about its southern pivot (Figure 8c,d). Strong ocean currents and winds coupled with a shallow seabed might have played a role in this turn of events. A68 has shown a tendency to alter its heading when in close proximity to the coastline of the Antarctic Peninsula. Perhaps this is due to a combination of high ice rises in the winter coupled with the shallow seabed. The rotation about its newfound southern fulcrum continued until July 2019, at which point A68 was nearly parallel to the Antarctic Circle (Figure 9b). By September 2019, the center of A68 had rotated nearly 40 degrees in a counter-clockwise direction (Figures 9d and 14a,b). From here on, its northward journey began in earnest, with the center having traveled a distance of 132.49 km by the end of 2019, 2/3rd of which was covered in December alone. At this point, A68's time in the Weddell Sea was almost over and its heading into the open ocean had commenced (Figure 10).

The year 2020 saw A68 heading northwards by leaps and bounds. By January 2020, it had steadied itself to a nearly upright position with the major axis rotating by ~30 degrees and positioning itself almost perpendicular to the Antarctic Circle (Figure 11). Here on, A68 continued northward, propelled by wind and ocean currents until November 2020 with the singular calving of A68C in April 2020 (Figures 10e and 11a). The real action started in the latter half of December 2020, when A68A gave rise to three more fragments (Figure 12a) with the closest one, namely A68D, the smallest out of these newly formed icebergs, standing at a mere 65.35 km from the South Georgia and South Sandwich Islands. A68A was a bit further out at 123 km from the islands. A68E and A68F formed from calving at roughly the minor axis of A68A, with A68E taking with it P7′ (Figure 12b). While A68D remained somewhat in the vicinity of the islands, A68E drifted north-eastwardly by the first week of January (Figure 12b).

By 29 January, another calving event gave rise to more company for the recently reduced A68A, by forming A68G and A68H (Figure 12c). At this point, A68 stood at roughly 56.5° S and 36° W.

The given diagram (Figure 15) shows the total distance covered by iceberg A68 from emergence to end, the changes in its shape, and the breakup of A68 into ice blocks over time.

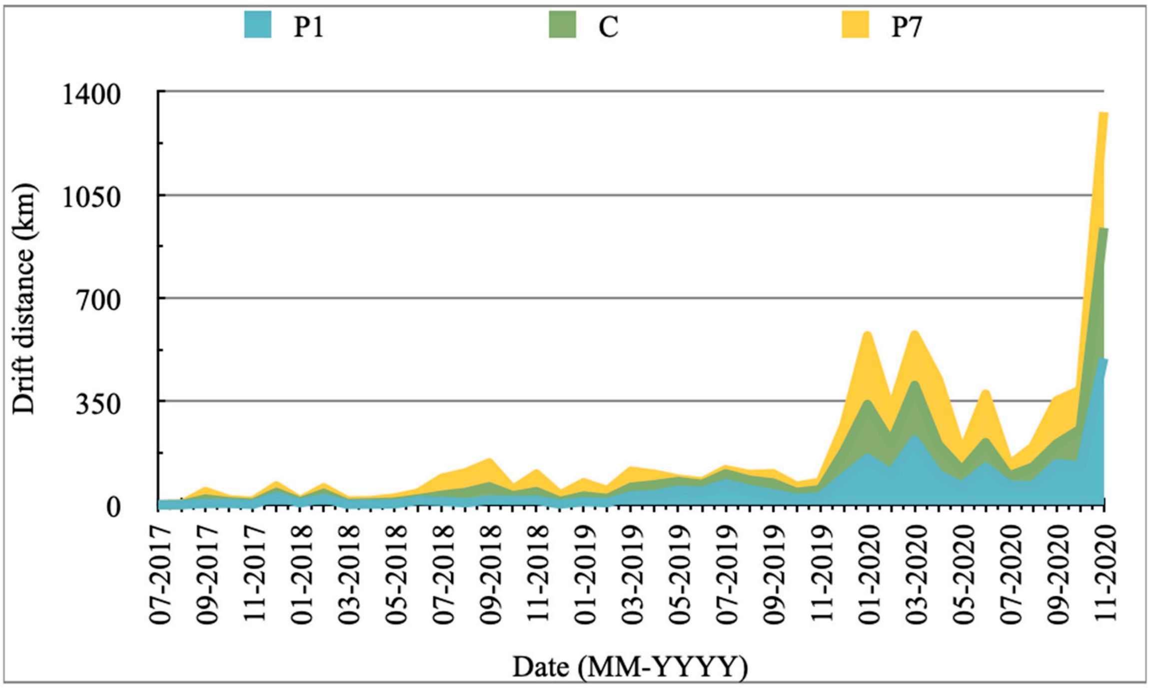

(**a**)

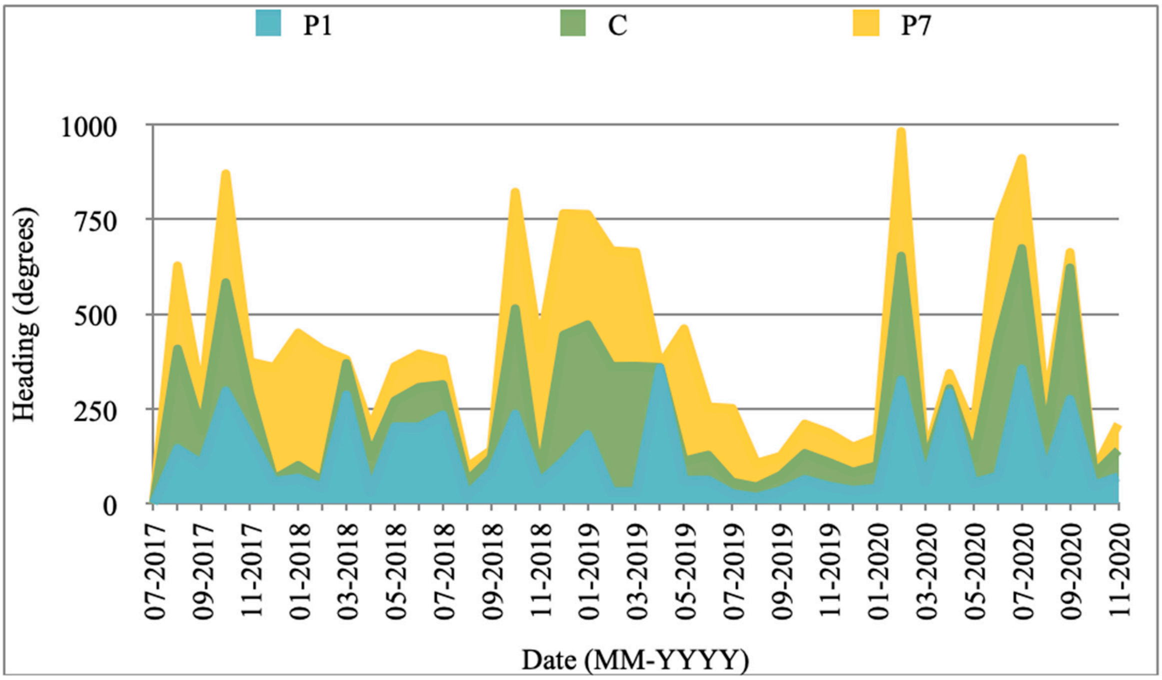

(**b**)

Figure 14. (**a**) Changes in the drift distance traveled by iceberg A68A's north, center, and southern portions, namely, P1(P1′), C, and P7, respectively. (**b**) Changes in the heading (direction) of iceberg A68A's locations P1(P1′), C, and P7 (0° = from the south, 90° = from the west, 180° = from the north, 270° = from the east).

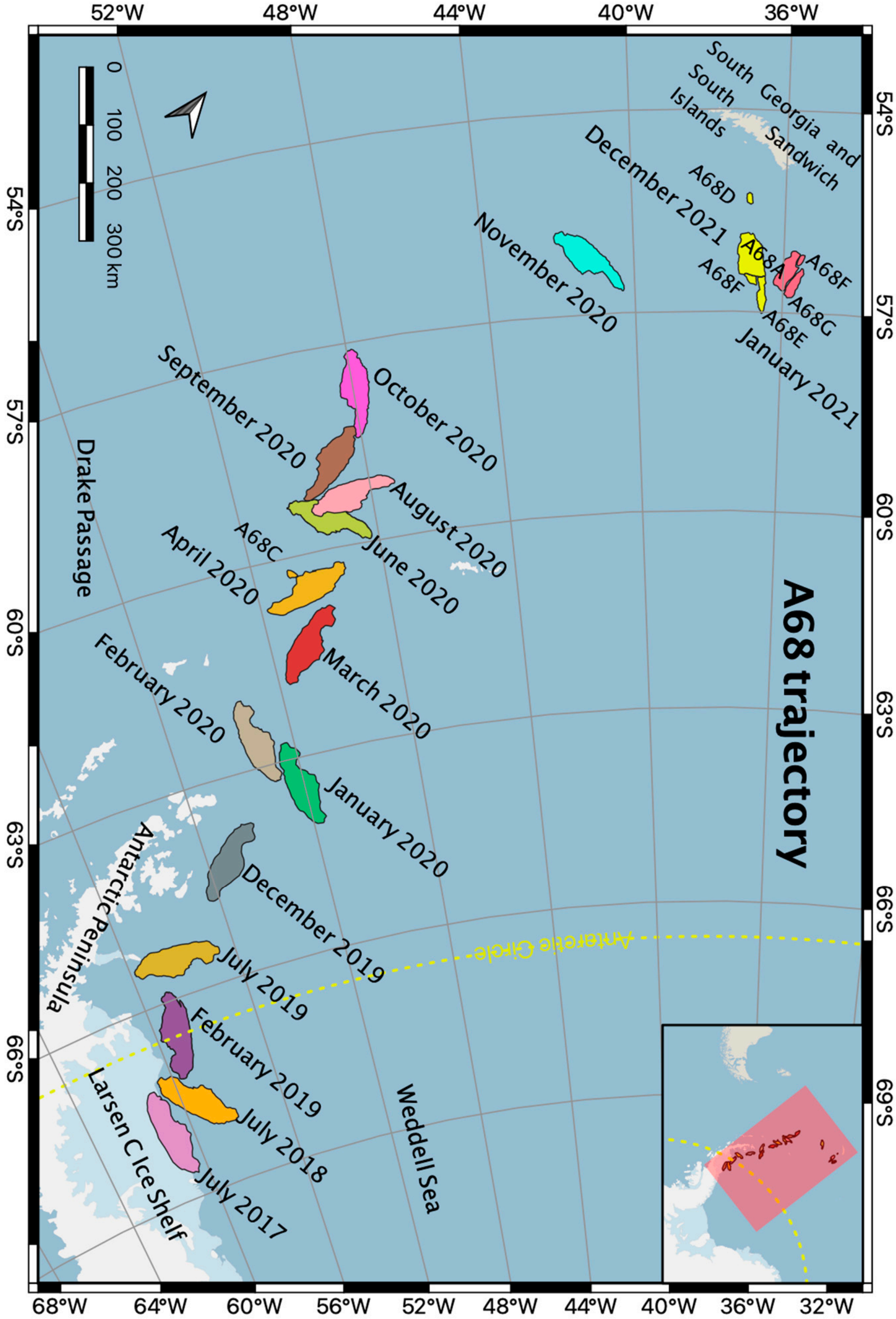

Figure 15. A68 trajectory from 27 July 2017 to 29 January 2021.

4. Conclusions

Analysis of A68's evolution through a span of almost 3 years reveals the basic mechanisms through which tabular icebergs as large as A68 move and change. As expected, during the first few months of its birth, A68 rattled around the bay-shaped region where it was birthed. The added dynamic of the shallow seabed of more than −300 m near the Bawden Ice Rise made it difficult for A68 to escape the clutches of its place of origin. It ultimately managed to escape dramatically by acting as a class 3 lever. While not a perfect analogy, it did change its fulcrum, largely due to a combination of the shallow seabed and momentum built through rotation. It also underwent further calving twice, in March 2019 (Figure 8b) and April 2020 (Figure 10e), although a significant portion (80%), it is still intact and is expected to remain so for some months. It is also abundantly clear that sea ice has a part to play in facilitating the longitudinal stretching of the iceberg by its absence during the summer season. Of noteworthy mention is the reduction in radar backscatter from the iceberg surface during the summer season, direct proof of surface melt atop the iceberg.

The results surmised here suggest that the trajectory of gargantuan icebergs, such as A68 does not simply depend on ocean currents and wind speed (and direction). Their scale and size make them much more susceptible to undulations of the coastal region, be it shallow seabed or ice rises. This may give rise to novel movements and unexpected drifts as far as iceberg motion is concerned. Although once free from the floundering movements in the coastal slope and out into the open sea, they may pick up the pace and perhaps join the iceberg highway, as is expected from icebergs in the region. It is of acute concern to study and generalize these motions, since the enmeshment of icebergs in the coastal region and/or near ice sheets, whether by grounding or cumbrous motion, could lead to interesting glaciological, oceanic, and ecological repercussions. Coastal trapping could have an effect on icebergs discharged into the ocean where freshwater flux leads to overturning circulation (e.g., the North Atlantic during glacial times) by mitigating the circulation knock-down effect associated with ice sheet discharge [58–60].

Author Contributions: Conceptualization, S.K., S.S. and N.K.; methodology, S.S. and S.K.; software, S.S. and S.K.; validation, S.S. and S.K.; formal analysis, S.S. and S.K; investigation, S.S. and S.K.; resources, S.K.; data curation, S.K.; writing—original draft preparation, S.S.; writing—review and editing, S.K., S.S. and N.K.; visualization, S.S. and S.K.; supervision, S.K.; project administration, S.K. All authors have read and agreed to the published version of the manuscript.

Funding: This research received no external funding.

Institutional Review Board Statement: Not applicable.

Informed Consent Statement: Not applicable.

Data Availability Statement: Sentinel-1 SAR data is freely available and can be searched and downloaded from the Copernicus Open Access Hub (formerly known as the Sentinels Scientific Data Hub) and Alaska Satellite Facility (ASF). Sentinel-1 GRDM products are available at the following links: https://scihub.copernicus.eu/dhus/#/home; https://search.asf.alaska.edu/#/.

Acknowledgments: The authors would like to express their sincere gratitude to the software support team of ESA for providing SNAP 8.0 tool for polarimetric processing of the SAR data. The authors are thankful to the Copernicus Open Access Hub for the Sentinel-2 optical multispectral data. The authors would also like to thank the project team of the Quantarctica (QGIS, «Quantum GIS» + Antarctica = Quantarctica is a collection of Antarctic geographical datasets for research, education, operations, and management in Antarctica) package for generating Figures 4–12 and 15. The SNAP tool and the Quantarctica package are available at the following links: SNAP Software: https://step.esa.int/main/download/snap-download/; Quantarctica package: https://www.npolar.no/quantarctica/.

Conflicts of Interest: The authors declare no conflict of interest.

Appendix A

Table A1. Sentinel-1 A/B data used in this study.

Date	Satellite/Acquisition Mode	Pass	Product
27 July 2017	S1-A/EW	Ascending	S1A_EW_GRDM_1SSH_20170727T002304_20170727T002404_017649_01D8BC_C976
3 August 2017	S1-A/EW	Ascending	S1A_EW_GRDM_1SSH_20170803T001459_20170803T001559_017751_01DBC9_F634
25 September 2017	S1-A/EW	Ascending	S1A_EW_GRDM_1SSH_20170925T002307_20170925T002407_018524_01F37A_0311
26 October 2017	S1-A/EW	Ascending	S1A_EW_GRDM_1SSH_20171026T001502_20171026T001602_018976_020126_F936
7 November 2017	S1-A/EW	Ascending	S1A_EW_GRDM_1SSH_20171107T001502_20171107T001602_019151_020690_D6E4
25 December 2017	S1-A/EW	Ascending	S1A_EW_GRDM_1SSH_20171225T001500_20171225T001600_019851_021C62_4E3F
25 January 2018	S1-B/EW	Ascending	S1B_EW_GRDM_1SDH_20180125T235803_20180125T235903_009334_010C0A_D6F0
24 February 2018	S1-A/EW	Ascending	S1A_EW_GRDM_1SSH_20180224T235845_20180224T235945_020755_023922_2621
25 March 2018	S1-B/EW	Ascending	S1B_EW_GRDM_1SDH_20180325T001417_20180325T001517_010180_0127F5_17C4
24 April 2018	S1-A/EW	Ascending	S1A_EW_GRDM_1SSH_20180424T001500_20180424T001600_021601_0253BE_8BC2
25 May 2018	S1-B/EW	Ascending	S1B_EW_GRDM_1SDH_20180525T235806_20180525T235906_011084_01451D_2B57
30 June 2018	S1-B/EW	Ascending	S1B_EW_GRDM_1SDH_20180630T235808_20180630T235908_011609_01557E_7086
31 July 2018	S1-B/EW	Ascending	S1B_EW_GRDM_1SDH_20180731T235005_20180731T235103_012061_016359_71AA
28 August 2018	S1-B/EW	Ascending	S1B_EW_GRDM_1SDH_20180828T001425_20180828T001525_012455_016F83_4B18
22 September 2018	S1-B/EW	Ascending	S1B_EW_GRDM_1SDH_20180922T235812_20180922T235912_012834_017B29_8D97
28 October 2018	S1-B/EW	Ascending	S1B_EW_GRDM_1SDH_20181028T235813_20181028T235913_013359_018B4E_37AD
29 November 2018	S1-B/EW	Ascending	S1B_EW_GRDH_1SDH_20181129T075243_20181129T075343_013816_0199BA_7EEB
23 December 2018	S1-B/EW	Descending	S1B_EW_GRDH_1SDH_20181223T075243_20181223T075343_014166_01A531_6C6E
26 January 2019	S1-A/EW	Ascending	S1A_EW_GRDM_1SSH_20190126T235852_20190126T235952_025655_02D96F_A401
19 February 2019	S1-A/EW	Ascending	S1A_EW_GRDM_1SSH_20190219T235851_20190219T235951_026005_02E5F2_4A84
28 March 2019	S1-B/EW	Ascending	S1B_EW_GRDM_1SSH_20190328T235009_20190328T235113_015561_01D2B7_2B7C
26 April 2019	S1-A/EW	Descending	S1A_EW_GRDM_1SSH_20190426T080952_20190426T081100_026958_0308AE_2513
28 May 2019	S1-B/EW	Descending	S1B_EW_GRDM_1SDH_20190528T075244_20190528T075344_016441_01EF2D_3039
25 June 2019	S1-A/EW	Descending	S1A_EW_GRDM_1SSH_20190625T080955_20190625T081102_027833_032466_897E
31 July 2019	S1-A/EW	Descending	S1A_EW_GRDM_1SSH_20190731T080957_20190731T081105_028358_033457_13EA
20 August 2019	S1-B/EW	Descending	S1B_EW_GRDH_1SDH_20190820T075249_20190820T075349_017666_0213C3_F0A9
25 September 2019	S1-B/EW	Descending	S1B_EW_GRDH_1SDH_20190925T075250_20190925T075350_018191_02240E_D460
31 October 2019	S1-B/EW	Descending	S1B_EW_GRDH_1SDH_20191031T075250_20191031T075350_018716_02346C_B773
12 November 2019	S1-B/EW	Descending	S1B_EW_GRDM_1SDH_20191112T075250_20191112T075350_018891_023A13_5BFE
20 December 2019	S1-A/EW	Ascending	S1A_EW_GRDM_1SSH_20191220T232735_20191220T232835_030438_037BDA_8A3B
30 January 2020	S1-B/EW	Descending	S1B_EW_GRDM_1SDH_20200130T074327_20200130T074427_020043_025ECE_BC3C
28 February 2020	S1-B/EW	Descending	S1B_EW_GRDH_1SDH_20200228T075147_20200228T075247_020466_026C71_83C0
30 March 2020	S1-B/EW	Descending	S1B_EW_GRDM_1SDH_20200330T074327_20200330T074427_020918_027AC5_C291

Table A1. *Cont.*

Date	Satellite/Acquisition Mode	Pass	Product
29 April 2020	S1-A/EW	Ascending	S1A_EW_GRDM_1SSH_20200429T224716_20200429T224816_032348_03BE82_E107
3 May 2020	S1-B/EW	Ascending	S1B_EW_GRDH_1SSH_20200503T230242_20200503T230342_021423_028AB9_436B
23 May 2020	S1-A/EW	Ascending	S1A_EW_GRDM_1SSH_20200523T224717_20200523T224817_032698_03C996_8684
28 June 2020	S1-A/EW	Ascending	S1A_EW_GRDM_1SSH_20200628T224719_20200628T224819_033223_03D95B_CEDA
29 July 2020	S1-A/EW	Ascending	S1A_EW_GRDM_1SSH_20200729T223916_20200729T224016_033675_03E727_568B
28 August 2020	S1-A/EW	Ascending	S1B_EW_GRDM_1SSH_20200828T223836_20200828T223936_023129_02BEA9_A7FD
27 September 2020	S1-A/EW	Ascending	S1A_EW_GRDM_1SSH_20200927T223919_20200927T224019_034550_040586_0FBC
8 October 2020	S1-B/EW	Descending	S1B_EW_GRDM_1SDH_20201008T074232_20201008T074336_023718_02D11F_8F67
25 November 2020	S1-A/EW	Ascending	S1A_EW_GRDM_1SSH_20201125T215925_20201125T220025_035410_042365_957F
22 December 2020	S1-A/EW	Ascending	S1A_EW_GRDM_1SSH_20201222T071734_20201222T071834_035795_0430AC_13DF
5 January 2021	S1-A/EW	Ascending	S1A_EW_GRDM_1SSH_20210105T070105_20210105T070205_035999_0437A6_68B2
29 January 2021	S1-A/EW	Ascending	S1A_EW_GRDM_1SSH_20210129T070125_20210129T070225_036349_0443E7_153A
1 February 2021	S1-B/EW	Ascending	S1B_EW_GRDM_1SSH_20210201T214125_20210201T214229_025418_03070C_4DBB

References

1. Copland, L.; Mueller, D.R.; Weir, L. Rapid Loss of the Ayles Ice Shelf, Ellesmere Island, Canada. *Geophys. Res. Lett.* **2007**, *34*, 21501. [CrossRef]
2. Rignot, E.; Velicogna, I.; Van Den Broeke, M.R.; Monaghan, A.; Lenaerts, J. Acceleration of the Contribution of the Greenland and Antarctic Ice Sheets to Sea Level Rise. *Geophys. Res. Lett.* **2011**, *38*, L05503. [CrossRef]
3. Joughin, I.; Smith, B.E.; Medley, B. Marine Ice Sheet Collapse Potentially under Way for the Thwaites Glacier Basin, West Antarctica. *Science* **2014**, *344*, 735–738. [CrossRef] [PubMed]
4. Smith, K.L.; Sherman, A.D.; Shaw, T.J.; Sprintall, J. Icebergs as Unique Lagrangian Ecosystems in Polar Seas. *Ann. Rev. Mar. Sci.* **2013**, *5*, 269–287. [CrossRef] [PubMed]
5. Vernet, M.; Smith, K.L.; Cefarelli, A.O.; Helly, J.J.; Kaufmann, R.S.; Lin, H.; Long, D.G.; Murray, A.E.; Robison, B.H.; Ruhl, H.A.; et al. Islands of Ice: Influence of Free-Drifting Antarctic Icebergs on Pelagic Marine Ecosystems. *Oceanography* **2012**, *25*, 38–39. [CrossRef]
6. Stern, A.A.; Adcroft, A.; Sergienko, O. The Effects of Antarctic Iceberg Calving-Size Distribution in a Global Climate Model. *J. Geophys. Res. Ocean.* **2016**, *121*, 5773–5788. [CrossRef]
7. Bigg, G.R.; Wadley, M.R.; Stevens, D.P.; Johnson, J.A. Modelling the Dynamics and Thermodynamics of Icebergs. *Cold Reg. Sci. Technol.* **1997**, *26*, 113–135. [CrossRef]
8. Death, R.; Siegert, M.J.; Bigg, G.R.; Wadley, M.R. Modelling Iceberg Trajectories, Sedimentation Rates and Meltwater Input to the Ocean from the Eurasian Ice Sheet at the Last Glacial Maximum. *Palaeogeogr. Palaeoclimatol. Palaeoecol.* **2006**, *236*, 135–150. [CrossRef]
9. Martin, T.; Adcroft, A. Parameterizing the Fresh-Water Flux from Land Ice to Ocean with Interactive Icebergs in a Coupled Climate Model. *Ocean Model.* **2010**, *34*, 111–124. [CrossRef]
10. Jongma, J.I.; Driesschaert, E.; Fichefet, T.; Goosse, H.; Renssen, H. The Effect of Dynamic–Thermodynamic Icebergs on the Southern Ocean Climate in a Three-Dimensional Model. *Ocean Model.* **2009**, *26*, 104–113. [CrossRef]
11. Daley, C.; Veitch, B. *Iceberg Evolution Modelling: A Background Study*; NRC Publications Archive: Vancover, BC, Canada, 2000; pp. 20–53.
12. Smith, S.D.; Banke, E.G. The Influence of Winds, Currents and Towing Forces on the Drift of Icebergs. *Cold Reg. Sci. Technol.* **1983**, *6*, 241–255. [CrossRef]
13. Lichey, C.; Hellmer, H. Modeling Giant Iceberg Drift under the Influence of Sea Ice in the Weddell Sea. *J. Glaciol.* **2001**, *47*, 452–460. [CrossRef]
14. Keghouche, I.; Bertino, L.; Lisæter, K.A. Parameterization of an Iceberg Drift Model in the Barents Sea. *J. Atmos. Ocean. Technol.* **2009**, *26*, 2216–2227. [CrossRef]
15. Garrett, C.; Middleton, J.; Hazen, M.; Majaess, F. Tidal Currents and Eddy Statistics From Iceberg Trajectories off Labrador. *Science* **1985**, *227*, 1333–1335. [CrossRef] [PubMed]
16. Smith, S.D. Hindcasting Iceberg Drift Using Current Profiles and Winds. *Cold Reg. Sci. Technol.* **1993**, *22*, 33–45. [CrossRef]
17. Wagner, T.J.W.; Dell, R.W.; Eisenman, I. An Analytical Model of Iceberg Drift. *J. Phys. Oceanogr.* **2016**, *47*, 1605–1616. [CrossRef]
18. Han, H.; Lee, S.; Kim, J.-I.; Kim, S.H.; Kim, H. Changes in a Giant Iceberg Created from the Collapse of the Larsen C Ice Shelf, Antarctic Peninsula, Derived from Sentinel-1 and CryoSat-2 Data. *Remote Sens.* **2019**, *11*, 404. [CrossRef]
19. Parmiggiani, F.; Moctezuma-Flores, M.; Guerrieri, L.; Battagliere, M.L. SAR Analysis of the Larsen-C A-68 Iceberg Displacements. *Int. J. Remote Sens.* **2018**, *39*, 5850–5858. [CrossRef]
20. Wesche, C.; Dierking, W. Estimating Iceberg Paths Using a Wind-Driven Drift Model. *Cold Reg. Sci. Technol.* **2016**, *125*, 31–39. [CrossRef]
21. Yulmetov, R.; Marchenko, A.; Løset, S. Iceberg and Sea Ice Drift Tracking and Analysis off North-East Greenland. *Ocean Eng.* **2016**, *123*, 223–237. [CrossRef]
22. Frost, A.; Ressel, R.; Lehner, S. Automated Iceberg Detection Using High-Resolution X-Band SAR Images. *Can. J. Remote Sens.* **2016**, *42*, 354–366. [CrossRef]
23. Oliver, C.; Quegan, S. *Understanding Synthetic Aperture Radar Images*, 2nd ed.; SciTech Publishing Inc.: Boston, MA, USA, 2004; ISBN 1-891121-31-6.
24. Tao, D.; Anfinsen, S.N.; Brekke, C. Robust CFAR Detector Based on Truncated Statistics in Multiple-Target Situations. *IEEE Trans. Geosci. Remote Sens.* **2016**, *54*, 117–134. [CrossRef]
25. Al-Hussaini, E.K.; Al-Hussaini, E.K.; Ibrahim, B.M. Comparison of Adaptive Cell-Averaging Detectors for Multiple-Target Situations. *IEE Proc. F Commun. Radar Signal Process.* **1986**, *133*, 217–223. [CrossRef]
26. Barkat, M.; Himonas, S.D.; Varshney, P.K. CFAR Detection for Multiple Target Situations. *IEE Proc. Part F Commun. Radar Signal Process.* **1989**, *136*, 193–209. [CrossRef]
27. Crisp, D.J. *The State-of-the-Art in Ship Detection in Synthetic Aperture Radar Imagery*; DSTO Information Sciences Laboratory: Edinburgh, Australia, 2004.
28. Silva, T.A.M.; Bigg, G.R. Computer-Based Identification and Tracking of Antarctic Icebergs in SAR Images. *Remote Sens. Environ.* **2005**, *94*, 287–297. [CrossRef]
29. Wesche, C.; Dierking, W. Iceberg Signatures and Detection in SAR Images in Two Test Regions of the Weddell Sea, Antarctica. *J. Glaciol.* **2012**, *58*, 325–339. [CrossRef]

30. Williams, R.N.; Rees, W.G.; Young, N.W. A Technique for the Identification and Analysis of Icebergs in Synthetic Aperture Radar Images of Antarctica. *Int. J. Remote Sens.* **1999**, *20*, 3183–3199. [CrossRef]
31. Willis, C.J.; Macklin, J.T.; Partington, K.C.; Teleki, K.A.; Rees, W.G.; Williams, R.G. Iceberg Detection Using ERS-1 Synthetic Aperture Radar. *Int. J. Remote Sens.* **1996**, *17*, 1777–1795. [CrossRef]
32. Young, N.W.; Turner, D.; Hyland, G.; Williams, R.N. Near-Coastal Iceberg Distributions in East Antarctica, 50–145° E. *Ann. Glaciol.* **1998**, *27*, 68–74. [CrossRef]
33. Langley, K.; Hamran, S.-E.; Hogda, K.A.; Storvold, R.; Brandt, O.; Hagen, J.O.; Kohler, J. Use of C-Band Ground Penetrating Radar to Determine Backscatter Sources within Glaciers. *IEEE Trans. Geosci. Remote Sens.* **2007**, *45*, 1236–1246. [CrossRef]
34. Rignot, E.; Echelmeyer, K.; Krabill, W. Penetration Depth of Interferometric Synthetic-Aperture Radar Signals in Snow and Ice. *Geophys. Res. Lett.* **2001**, *28*, 3501–3504. [CrossRef]
35. Akbari, V.; Brekke, C. Iceberg Detection in Open and Ice-Infested Waters Using C-Band Polarimetric Synthetic Aperture Radar. *IEEE Trans. Geosci. Remote Sens.* **2018**, *56*, 407–421. [CrossRef]
36. Gill, R.S. Operational Detection of Sea Ice Edges and Icebergs Using SAR. *Can. J. Remote Sens.* **2001**, *27*, 411–432. [CrossRef]
37. Power, D.; Youden, J.; Lane, K.; Randell, C.; Flett, D. Iceberg Detection Capabilities of RADARSAT Synthetic Aperture Radar. *Can. J. Remote Sens.* **2001**, *27*, 476–486. [CrossRef]
38. Marino, A.; Dierking, W.; Wesche, C. A Depolarization Ratio Anomaly Detector to Identify Icebergs in Sea Ice Using Dual-Polarization SAR Images. *IEEE Trans. Geosci. Remote Sens.* **2016**, *54*, 5602–5615. [CrossRef]
39. Kim, J.-W.; Kim, D.; Kim, S.-H.; Hwang, B.-J. Iceberg Detection Using Full-Polarimetric RADARSAT-2 SAR Data in West Antarctica. In Proceedings of the 2011 3rd International Asia-Pacific Conference on Synthetic Aperture Radar (APSAR), Seoul, Republic of Korea, 26–30 September 2011; pp. 1–4.
40. Dierking, W.; Wesche, C. C-Band Radar Polarimetry—Useful for Detection of Icebergs in Sea Ice? *IEEE Trans. Geosci. Remote Sens.* **2014**, *52*, 25–37. [CrossRef]
41. Crocker, R.I.; Maslanik, J.A.; Adler, J.J.; Palo, S.E.; Herzfeld, U.C.; Emery, W.J. A Sensor Package for Ice Surface Observations Using Small Unmanned Aircraft Systems. *IEEE Trans. Geosci. Remote Sens.* **2012**, *50*, 1033–1047. [CrossRef]
42. Benn, D.I.; Åström, J.A. Calving Glaciers and Ice Shelves. *Adv. Phys. X* **2018**, *3*, 1048–1076. [CrossRef]
43. National Snow & Ice Data Center. National Snow and Ice Data Center—Advancing Knowledge of Earth's Frozen Regions. Available online: https://nsidc.org/ (accessed on 14 September 2021).
44. Scambos, T.A.; Bohlander, J.A.; Shuman, C.A.; Skvarca, P. Glacier Acceleration and Thinning after Ice Shelf Collapse in the Larsen B Embayment, Antarctica. *Geophys. Res. Lett.* **2004**, *31*, L18402. [CrossRef]
45. European Space Agency. Keeping an Eye on Wilkins Ice Shelf. Available online: https://www.esa.int/Applications/Observing_the_Earth/Keeping_an_eye_on_Wilkins_Ice_Shelf (accessed on 14 September 2021).
46. Rott, H.; Skvarca, P.; Nagler, T. Rapid Collapse of Northern Larsen Ice Shelf, Antarctica. *Science* **1996**, *271*, 788–792. [CrossRef]
47. Rignot, E.; Jacobs, S.; Mouginot, J.; Scheuchl, B. Ice-Shelf Melting around Antarctica. *Science* **2013**, *341*, 266–270. [CrossRef] [PubMed]
48. Massom, R.A.; Scambos, T.A.; Bennetts, L.G.; Reid, P.; Squire, V.A.; Stammerjohn, S.E. Antarctic Ice Shelf Disintegration Triggered by Sea Ice Loss and Ocean Swell. *Nature* **2018**, *558*, 383–389. [CrossRef] [PubMed]
49. Davies, B. The Larsen C Ice Shelf Growing Rift Antarctic Peninsula Ice Shelves. Available online: https://www.antarcticglaciers.org/2017/06/larsen-c-ice-rift/ (accessed on 15 November 2022).
50. Loff, S. Rift in Antarctica's Larsen C Ice Shelf. Available online: https://www.nasa.gov/image-feature/rift-in-antarcticas-larsen-c-ice-shelf (accessed on 15 November 2022).
51. Schannwell, C.; Cornford, S.; Pollard, D.; Barrand, N.E. Dynamic Response of Antarctic Peninsula Ice Sheet to Potential Collapse of Larsen C and George VI Ice Shelves. *Cryosphere* **2018**, *12*, 2307–2326. [CrossRef]
52. Booth, A.; Luckman, A.; White, J.; Pearce, E.; Cornford, S.; Kulessa, B.; Brisbourne, A.; Hubbard, B. Mechanical Response of Larsen C Ice Shelf Following the A68 Calving Event: Observations from Field-Based Geophysical Measurements. In Proceedings of the EGU General Assembly Conference, Vienna, Austria, 4–13 April 2018; p. 10049.
53. Arndt, J.E.; Schenke, H.W.; Jakobsson, M.; Nitsche, F.O.; Buys, G.; Goleby, B.; Rebesco, M.; Bohoyo, F.; Hong, J.; Black, J.; et al. The International Bathymetric Chart of the Southern Ocean (IBCSO) Version 1.0—A New Bathymetric Compilation Covering Circum-Antarctic Waters. *Geophys. Res. Lett.* **2013**, *40*, 3111–3117. [CrossRef]
54. Thomas, R.H. The Dynamics of Marine Ice Sheets. *J. Glaciol.* **1979**, *24*, 167–177. [CrossRef]
55. Walter, F.; O'Neel, S.; McNamara, D.; Pfeffer, W.T.; Bassis, J.N.; Fricker, H.A. Iceberg Calving during Transition from Grounded to Floating Ice: Columbia Glacier, Alaska. *Geophys. Res. Lett.* **2010**, *37*, L15501. [CrossRef]
56. Ren, D.; Leslie, L.M.; Lynch, M.J. Verification of Model Simulated Mass Balance, Flow Fields and Tabular Calving Events of the Antarctic Ice Sheet against Remotely Sensed Observations. *Clim. Dyn.* **2013**, *40*, 2617–2636. [CrossRef]
57. Liu, H.; Li, X.M.; Guo, H. The Dynamic Processes of Sea Ice on the East Coast of Antarctica—A Case Study Based on Spaceborne Synthetic Aperture Radar Data from TerraSAR-X. *IEEE J. Sel. Top. Appl. Earth Obs. Remote Sens.* **2016**, *9*, 1187–1198. [CrossRef]
58. Ganopolski, A.; Rahmstorf, S. Rapid Changes of Glacial Climate Simulated in a Coupled Climate Model. *Nature* **2001**, *409*, 153–158. [CrossRef]

59. Hemming, S.R. Heinrich Events: Massive Late Pleistocene Detritus Layers of the North Atlantic and Their Global Climate Imprint. *Rev. Geophys.* **2004**, *42*, RG1005. [CrossRef]
60. Macayeal, D.R.; Okal, M.H.; Thom, J.E.; Brunt, K.M.; Kim, Y.-J.; Bliss, A.K.; Macayeal, D.R.; Okal, M.H.; Thom, J.E.; Brunt, K.M.; et al. Tabular Iceberg Collisions within the Coastal Regime. *J. Glaciol.* **2008**, *54*, 371–386. [CrossRef]